



JAMES | Journal of Advances in Modeling Earth Systems*



RESEARCH ARTICLE

10.1029/2024MS004864

Key Points:

- LES models show consistent early cloud clustering among themselves, but differ from GOES16 observations in timing and structure
- Maxima in integrated cloud water and the onset of cold pools tend to precede the maximum cloud size of the Flowertype organization
- Flower formation occurs for a wide range of cloud droplet number concentrations, with highest concentration producing largest Flowers

Correspondence to:

G. N. Raghunathan, g.raghunathan@csuohio.edu

Citation:

Raghunathan, G. N., Blossey, P., Boeing, S., Denby, L., Ghazayel, S., Heus, T., et al. (2025). Flower-type organized trade-wind cumulus: A multi-day Lagrangian large eddy simulation intercomparison study. *Journal of Advances in Modeling Earth Systems*, *17*, e2024MS004864. https://doi.org/10.1029/2024MS004864

Received 26 NOV 2024 Accepted 10 SEP 2025

© 2025 The Author(s). Journal of Advances in Modeling Earth Systems published by Wiley Periodicals LLC on behalf of American Geophysical Union. This is an open access article under the terms of the Creative Commons Attribution License, which permits use, distribution and reproduction in any medium, provided the original work is properly cited.

Flower-Type Organized Trade-Wind Cumulus: A Multi-Day Lagrangian Large Eddy Simulation Intercomparison Study

Girish Nigamanth Raghunathan¹, Peter Blossey², Steven Boeing³, Leif Denby^{3,4}, Salima Ghazayel⁵, Thijs Heus¹, Jan Kazil⁶, and Roel Neggers⁵

¹Cleveland State University, Cleveland, OH, USA, ²University of Washington, Seattle, WA, USA, ³University of Leeds, Leeds, UK, ⁴Danish Meteorological Institute, Copenhagen, Denmark, ⁵University of Cologne, Cologne, Germany, ⁶Blue Earth Analytics, Lafayette, CO, USA

Abstract Shallow cumulus cloud fields in subtropical marine trade wind environments, particularly over the tropical Atlantic Ocean, show distinct organizational patterns. Among these, Flower-type clouds are characterized by expansive stratiform cloud patches surrounded by regions of scattered convection. The objectives of this study were (a) to construct a case study of a time period during the EUREC⁴A/ATOMIC field campaign when Flower-type organization was observed, (b) to evaluate the fidelity of a multi-model ensemble of large eddy simulations of that case, and (c) to analyze the interaction between cloud and precipitation processes and mesoscale organization in the simulations. The simulations follow a quasi-Lagrangian trajectory, allowing mesoscale features to develop over time in a domain that follows the boundary-layer airmass. The results show a broad agreement in simulated thermodynamic properties across different LES codes, with Flower-type cloud patches appearing within hours of each other. The consensus among models is consistent with observations made during the EUREC⁴A/ATOMIC field campaign on the specific day of interest. The cloud structure reveals three distinct peaks in the joint probability densities of cloud base and cloud top height, with the dominant peak at any given time influenced by the stage of cloud organization. The simulated cloud system evolution reveals consistent occurrence of maxima in liquid water path and rain rate before Flower reaches its maximum length scale. Targeted sensitivity tests reveal a weak relationship between Cloud Droplet Number concentration and the extent/degree/type of organization.

Plain Language Summary Oceanic clouds often form in distinct organizational patterns. In the North Atlantic trade winds near Barbados, satellite studies have classified these patterns into four types. Among them Flowers appear as clumped cloud patches, sometimes spanning over 100 km. This research aims to (a) study a specific Flower cloud event, (b) assess model accuracy in recreating it, and (c) analyze the role of meteorological conditions and cloud-rain patterns in its formation and growth. Simulations tracked an air column as Flower clouds formed, showing models recreated them accurately and matched satellite images from that day. Within the cloud patch, three cloud types emerge, evolving as Flower clouds form, grow, and decay. Results show that total cloud water and the spread of cool, dense surface air from rain evaporation peaked before the cloud patches reached their largest sizes. Sensitivity tests revealed that changes in cloud droplet concentrations had little effect on Flower cloud formation, except at very low concentrations where persistent rain hindered organization.

1. Introduction

Clouds forming in the marine boundary layer are a major source of uncertainty in global climate models (GCMs) due to their sensitivity to changing environmental conditions (Bony & Dufresne, 2005). These uncertainties stem from inconsistencies in representing their responsiveness to moisture variations and above-cloud stability characteristics, leading to errors in the estimated cloud cover (Medeiros & Nuijens, 2016). Shallow cumulus clouds in oceanic trade wind regions have played a leading role in the diversity of cloud feedbacks within GCMs (Vial et al., 2018). High resolution large eddy simulations, which represent cloud-scale circulations explicitly, show greater agreement in the sign and strength of shallow cumulus cloud feedbacks compared to GCMs (Blossey et al., 2016), though in idealized simulations with time-invariant meteorological conditions that represent a small sample of the variability seen in these regions.

Though long recognized in observations (Malkus & Riehl, 1964), the mesoscale organization of shallow cumulus clouds was not represented in many large eddy simulations of shallow cumulus clouds (e.g., Blossey et al., 2016)

RAGHUNATHAN ET AL. 1 of 29

due to computational constraints on the domain size. However, more recent studies using larger domain sizes (e.g., Vogel et al., 2016) found that mesoscale organization affects precipitation onset and the mean state of the boundary layer, and vice versa. As mesoscale organization may play a role in the response of these clouds to climate (Kazil et al., 2024; Nuijens & Siebesma, 2019), it has become important to accurately represent shallow cumulus convection and its distinct patterns of organization in such high-resolution models. Recently, mesoscale patterns found in downstream trades were classified, identifying four reproducible patterns (Sugar, Gravel, Fish, and Flowers) from 10 years of satellite images manually (Stevens et al., 2020), and using a supervised deep learning algorithm (Rasp et al., 2020), revealing significant seasonal and physical differences among them. These four mesoscale patterns were also found to correlate with large-scale environmental conditions in the region, such as near-surface wind speed and lower-tropospheric stability (Bony et al., 2020).

Among the observed types of organization, Flowers are distinguished by large, distinct stratiform cloud patches spread out and separated by areas of scattered convection. In some cases, these individual patches can extend over 100 km, leading to extensive cloud cover and a significant cloud radiative effect. These clouds are typically observed under strong near-surface winds ($v > 8 \text{ ms}^{-1}$), a more stable environment and colder sea surface temperatures (≈ 26°C) compared to other organized cloud types (Bony et al., 2020). Analyzing backward trajectories showed that Flowers form under consistently colder sea surface temperatures, persistently high Lower Tropospheric Stability (LTS), and significantly dry free troposphere conditions (Schulz et al., 2021). Sometimes, they can produce intense precipitation, triggering strong cold pools (Vogel et al., 2021a), which form due to downdrafts that bring colder, drier air to the surface (Zuidema et al., 2012). The EUREC⁴A (Elucidating the role of clouds-circulation coupling in climate) and ATOMIC (Atlantic Tradewind Ocean-Atmosphere Mesoscale Interaction Campaign) joint field campaign that took place between January-March 2020 was designed to understand the connections between the diverse types of shallow cumulus clouds in the region, the environmental conditions and the large-scale circulation, including a focus on testing hypotheses about how shallow cumulus respond to climate change (Stevens et al., 2021). This resulted in extensive measurements of shallow cumulus clouds in the region using remote sensing and in situ observations from research aircraft and ships, along with land-based instruments on Barbados.

High-resolution output produced by large eddy simulations has in the past been used by studies to address gaps left by observations. Early computational work on mesoscale organization in LES (Seifert & Heus, 2013) highlighted the role of precipitation and cold pools in shaping cloud patterns that resemble the "Gravel" organizational pattern of Stevens et al. (2020). Using idealized large eddy simulations of marine shallow cumulus convection, others (Bretherton & Blossey, 2017; Janssens, de Arellano, et al., 2023) have highlighted the propensity for mesoscale moisture anomalies of water vapor to be amplified by mesoscale circulations that are driven by anomalously strong convection in the moist region. This positive feedback on mesoscale moisture anomalies occurs even in the absence of precipitation (Bretherton & Blossey, 2017), though some caution should be taken with quantitative predictions because the growth rate of the moisture anomalies is sensitive to the details of numerical methods and grid spacing (Janssens, Vilà-Guerau de Arellano, et al., 2023). Cloud organization develops along airmass trajectories, possibly due to the influence of both larger-scale motions and these local processes. Quasi-Lagrangian simulations, in which the simulation domain is advected by winds within the boundary layer, have been used in idealized studies of cloud transitions (Bretherton et al., 1999; Sandu & Stevens, 2011), cloud-aerosol interactions (Yamaguchi et al., 2017), cloud feedbacks (Bretherton & Blossey, 2014) and the varying performance of climate model parameterizations in simulating cloud transitions (Neggers et al., 2017). More recently, simulations with quasi-Lagrangian forcing derived from reanalysis have been used to test the realism with which cloud transitions in the Southeast Atlantic can be represented (Kazil et al., 2021) and to identify the mechanisms driving Flower cloud organization during EUREC4A/ATOMIC (Narenpitak et al., 2021). In addition, by comparing evolving cloud organization across an ensemble of quasi-Lagrangian large eddy simulations, this work builds on previous work of previous model intercomparisons that have contributed to greater understanding of shallow cumulus convection (Siebesma et al., 2003; VanZanten et al., 2011) and of cloud evolution and transitions along quasi-Lagrangian trajectories (Bretherton et al., 1999; de Roode et al., 2016, 2019; Van der Dussen et al., 2013).

Past studies have explored the particular day during which large Flowers were observed (February 2nd, 2020) from the standpoint of observations (Cui et al., 2023; Schulz & Stevens, 2023) and simulations (Dauhut et al., 2023; Narenpitak et al., 2021; Saffin et al., 2023; Schulz & Stevens, 2023). Simulation-based studies, while

RAGHUNATHAN ET AL. 2 of 29

successful in reproducing Flower clouds closely resembling observations, have faced challenges with discrepancies in the timing of transitions (Narenpitak et al., 2021; Saffin et al., 2023), total cloud cover (Schulz & Stevens, 2023), and cloud-top height distribution (Dauhut et al., 2023). In studies using a single model, pinpointing the source of these discrepancies can be difficult, as results may still be affected by particular numerical or physical modeling decisions. To gain deeper insights, a close comparison of a specific, relevant case simulated using multiple independent codes may be necessary. Some of these past studies (Bony et al., 2020; Schulz et al., 2021) while investigating the large-scale factors influencing Flower formation found that stronger wind speeds and larger values of lower tropospheric stability were favorable conditions, while process studies (Alinaghi et al., 2024; Dauhut et al., 2023) highlighted the critical role of downdrafts and cold pools in the development and maintenance of Flower clouds. Alinaghi et al. (2024), for instance, emphasized the role of cold pools and the deep, cloudy updrafts along their edges in sustaining the organized state.

The primary goal of this study is to design a model intercomparison that enables each LES code to use its own distinct combination of numerical methods, microphysical schemes, and subgrid-scale parameterizations, while simulating a particular day when Flower clouds were observed. For this purpose, we use a similar case to Narenpitak et al. (2021), but with an extended lead time of 2 days prior to the day when Flower clouds were observed. The extended lead time allows for tracking of air mass through multiple cloud transitions as well as providing sufficient time for mesoscale moisture accumulation to occur. For this study, we focus on addressing the following questions: How do different LES codes compare in terms of timing and magnitude of simulated Flower clouds? What are the key factors that contribute to the formation of Flowers? How do differences in timing of precipitation development in a model stemming from differences in its microphysics affect the timing and scale of Flowers? How sensitive are Flowers to some of these crucial parameters and when do they encourage or inhibit the formation of Flowers? Do differences in thermodynamic properties among LES codes lead to large differences in the length and/or time scales of Flowers?

The article is organized as follows: Section 2 covers the simulation setup, including constraints and the derivation of boundary conditions and forcings for a Lagrangian trajectory, as well as the configuration of individual LES codes. Section 3 presents the results from multi-model LES simulations for the February 2nd case, analyzing overall thermodynamic and cloud properties, comparing them with satellite and ship-based radiosonde observations, and detailing the evolution of cloud structure as it transitions to the Flower pattern during the day. Section 4 investigates how changes in Cloud Droplet Number Concentration, simulation lead time, and random initial condition perturbations affect the timing and scale of Flowers. Finally, Section 5 provides a summary of the results, highlights key findings, and suggests directions for future research.

2. Data and Methodology

In this study, the results are presented based on four different LES models (SAM, MicroHH, DALES, and MONC) with two versions of SAM used by two different participating research groups (referred from here-on as SAM-NOAA and SAM-UW). The analysis period is centered around February 2nd, a day during which ubiquitous presence of Flower-type organized convection was observed over the region where the joint EUREC⁴A—ATOMIC joint field campaign took place.

The simulation trajectory as well as the forcing and boundary conditions were computed using Lagtraj (a code developed by co-authors at University of Leeds to extract ERA5 profiles along the lagrangian trajectory). This is done by tracking air mass backward from 500 m height right above the location of Ronald H. Brown research vessel deployed as a part of the EUREC 4 A—ATOMIC joint field campaign (stationed at 13.9 N, 54.5 W at 17 UTC). The resulting trajectory (which is similar to the trajectory used in Narenpitak et al. (2021) but with a 48-hr longer lead time) along with the corresponding sea surface temperature, large-scale pressure velocity, as well as the temperature and moisture advection profiles are shown in Figure 1. The trajectories, boundary conditions and forcing profiles were calculated based on ERA5 reanalysis data set averaged within a $2^{\circ} \times 2^{\circ}$ grid centered around computed latitude and longitude centers for calculating large-scale conditions. George et al. (2023) showed that the mesoscale winds in ERA5 are representative, and although Lagtraj does not directly incorporate the dropsonde measurements (George et al., 2021) from the campaign, these are assimilated into ERA5. Figure 1f shows the surface velocity distribution right around the time Flowers were starting to form. We can see generally north-easterly winds around the region of simulation trajectory that, along with the trajectory itself, change in direction to a more easterly wind with a larger magnitude as the day progresses. Corresponding GOES-16 satellite

RAGHUNATHAN ET AL. 3 of 29

from https://agupubs.onlinelibrary.wiley.com/doi/10.1029/2024MS00.4864 by NICE, National Institute for Health and Care Excellence, Wiley Online Library on [13/10/2025]. See the Terms and Condition

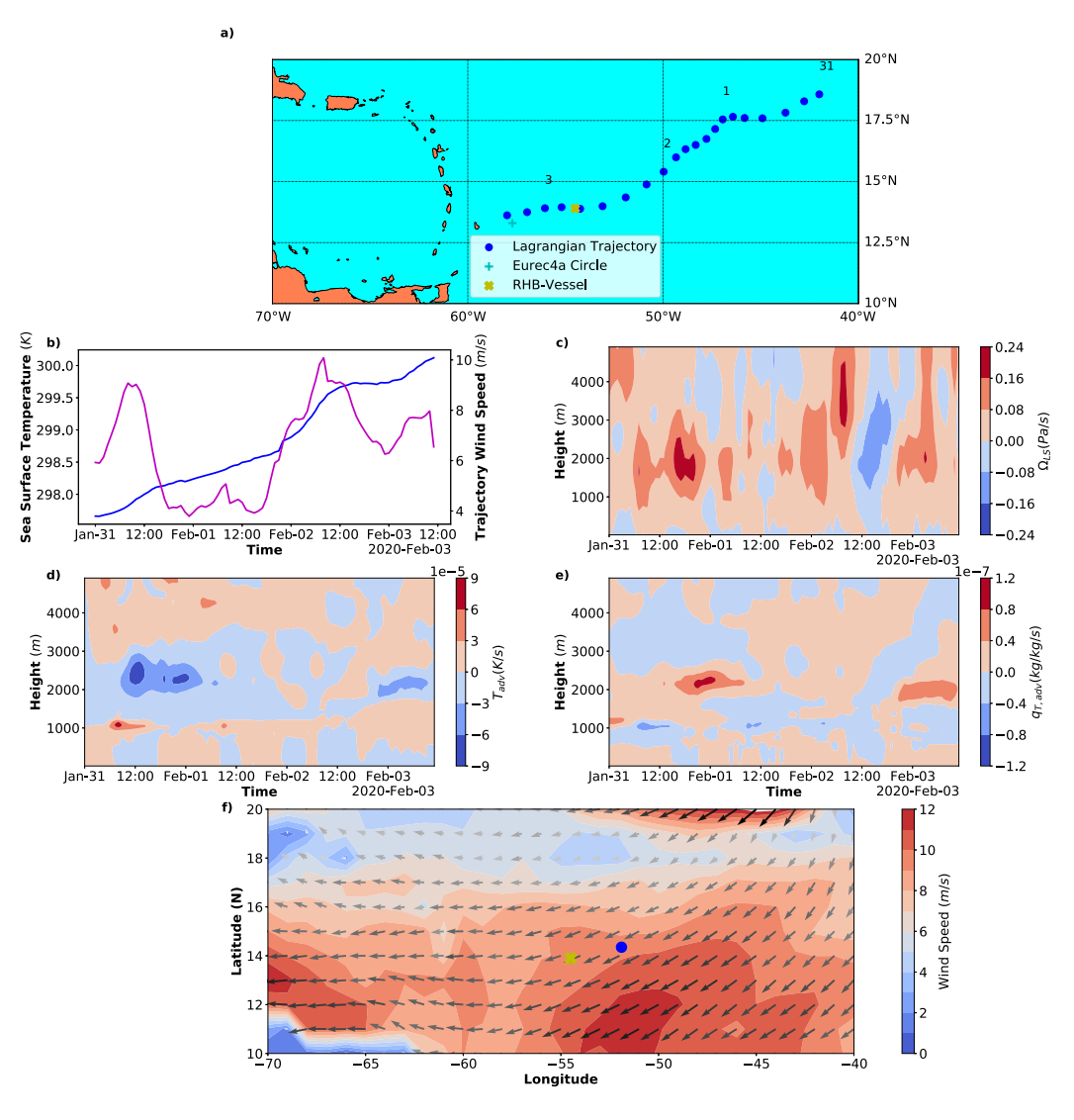


Figure 1. (a) Lagrangian trajectory centers computed for the control simulation shown every 4 hr between 00 UTC January 31st and 12 UTC February 3rd UTC (blue dots), along with the location of Ronald H. Brown shipping vessel (at 17 UTC on February 2nd, marked by a yellow cross), (b) Sea surface temperature (K), (c) Large scale pressure velocity Ω_{LS} (Pa/s), (d) Time-height cross-section of temperature advection and (e) Total water mixing ratio advection all of which were derived along the Lagrangian trajectory from ERA5 using Lagtraj, (f) Surface velocity magnitude contour (derived from ERA5) along with quiver lines indicating its direction over the region at 08 UTC on February 2nd and blue and yellow markers indicating Lagrangian trajectory center and RHB vessel position at that time.

imagery during the day (Figure 2) shows formation of Flower-like cloud patches emerging in the vicinity of the trajectory as early as 12 UTC with more prominent structures observed within the simulation domain itself as the trajectory draws closer to the site of RHB vessel.

The ERA5 reanalysis, used for initializing LES simulations, provides a best estimate of the atmosphere but is subject to biases arising from the underlying model. Beesley et al. (2000) for instance, while comparing one of the earlier ECMWF forecast models with observations, found large discrepancies in surface temperature. More recently, Schulz and Stevens (2023) identified a certain cold-bias in ERA5 sea surface temperatures over the EUREC⁴A circle region when compared to radiosonde observations ($\approx 0.4~K$) which leads to a potentially cooler and drier boundary layer in their simulations. Savazzi et al. (2022) found systematic lower-tropospheric wind biases in ERA5 around the EUREC4A field campaign region, with RMSEs of up to 2 m s⁻¹ and a mean wind bias of about $-0.5~m~s^{-1}$, even with the assimilation of sondes. Despite this, given the lack of required observational output over an extended region surrounding the EUREC⁴A field campaign site to conduct a Lagrangian study, we

RAGHUNATHAN ET AL. 4 of 29

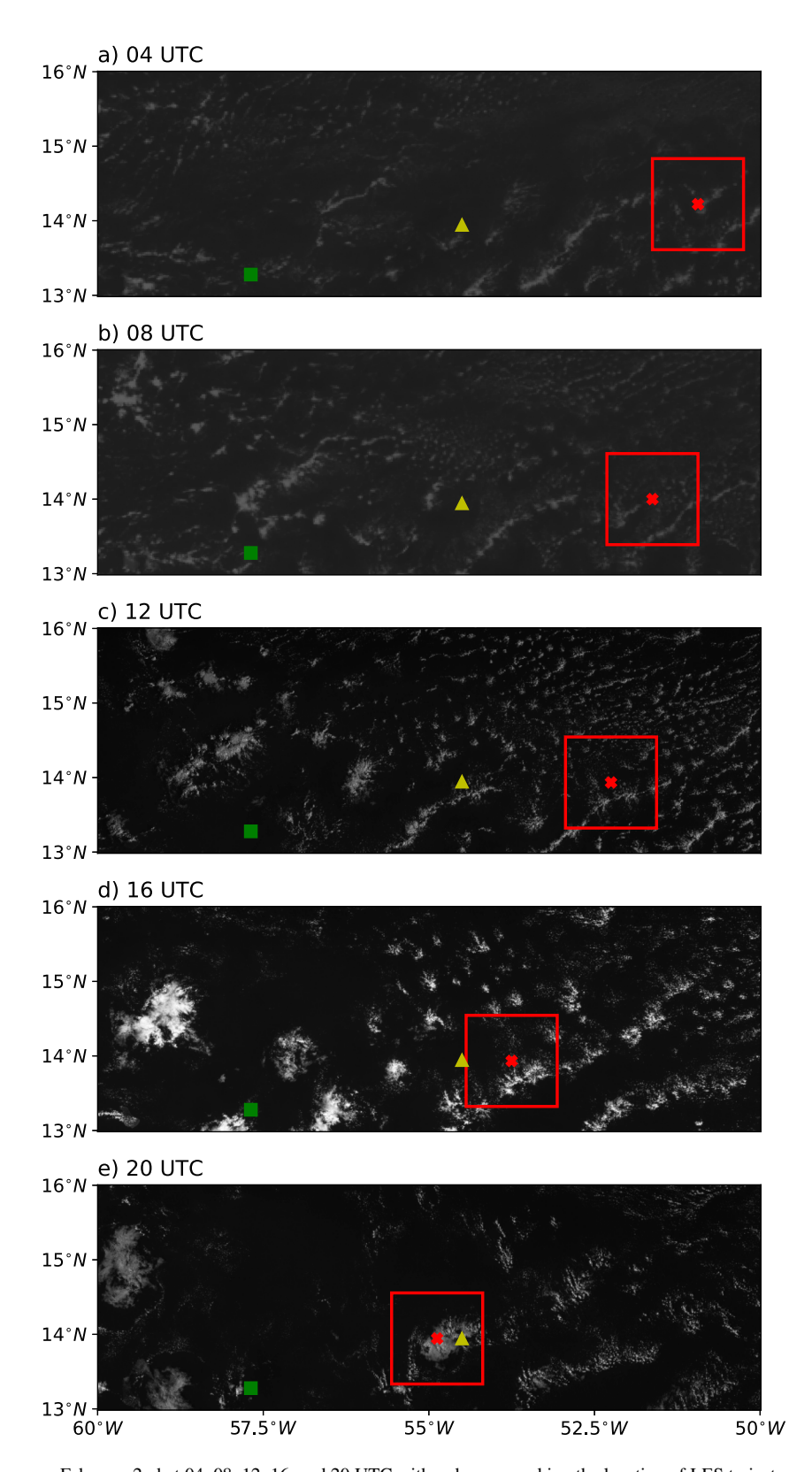


Figure 2. GOES satellite images on February 2nd at 04, 08, 12, 16, and 20 UTC with red cross marking the location of LES trajectory at corresponding times, yellow triangle indicating the location of RHB vessel and green square marking the center of EUREC⁴A HALO circle. GOES-16 imagery is displayed using Band 2 (visible, daytime) at 12, 16, and 20 UTC, with reflectance ranging from 0 to 0.8. For 04 and 08 UTC, Band 13 (infrared, nighttime) is used, showing brightness temperatures between 240 and 302 K. The data are visualized with continuous color shading using a colormap scaled between the specified minimum and maximum values.

RAGHUNATHAN ET AL. 5 of 29

rely on ERA5 in determining the trajectory as well as for providing surface and initial conditions. Thus, we proceed with using ERA5 for our simulations, acknowledging that some of the discrepancies with observations might be an artifact of inherent model biases.

2.1. Simulation Setup

The control simulations were initialized at 00 UTC 31st January 2020 with a total of 65 hr lead time before the trajectory intersects with the location of Ronald H. Brown research vessel and is allowed to continue for another 19 hr past this with a total runtime of 84 hr. Simulations were performed on a 153.6 \times 153.6 \times 8.5 km domain with a 150 m horizontal grid spacing ($\Delta x, \Delta y$) and a variable vertical grid spacing (Δz) which increases geometrically from 20 m (with first level at 10 m) at the surface to 40 m at 400 m height, stays constant at 40 m up to 5 km height and then increases geometrically beyond that up to 8.5 km. Observations showed cloud tops up to 3.5 km on Flower days (and up to 5 km on few other days associated with Fish or Gravel type cloud organization (Schulz & Stevens, 2023)), so we used a relatively high domain top with exponentially increasing grid spacing above 5 km to provide a turbulence buffer at minimal computational cost. Despite the grid's high anisotropy, a coarse horizontal resolution was chosen to maximize domain size and manage computational cost, as preliminary simulations with 100 and 50 m horizontal grid spacings (not shown) showed minimal impact on Flower length scale and timing compared to the results from current setup.

The sea surface temperature was prescribed, with interactive heat and moisture fluxes. An assumption of 98% saturation for surface humidity was made to account for sea surface salinity, with the presence of dissolved salts in the ocean reducing the overall evaporation. This 98% factor was then applied to the saturation specific humidity derived from sea surface temperature, to determine the surface humidity values. The models use doubly periodic boundary conditions with surface fluxes of heat and momentum and radiative heating rates computed interactively. A diurnal cycle of insolation is included, with the zenith angle a function of latitude and longitude, which changes during the simulation. The models apply a Galilean transform with a fixed velocity of (U,V)=(-6,-1) m s⁻¹. The initial temperature, humidity, and velocity profiles were specified using ERA5 data along the vertical axis at 00 UTC on 31 January 2020. Large-scale advective tendencies of heat, moisture, and momentum were prescribed. The Lagrangian setup of the simulations minimized large-scale advection of these variables, though variability of advection with height still exists and is prescribed. In some models (SAM-UW, SAM-NOAA, and DALES), momentum, temperature, and moisture are nudged above 5 km with a timescale of 1 hr to mitigate inertial oscillations in the upper troposphere. A fixed cloud droplet number concentration of 400 cm⁻³ was used by most models (except SAM-NOAA), based on CCN measurements made during the EUREC⁴A field campaign (Royer et al., 2023).

While the simulation domain only extends to 8.5 km, radiation is computed above that level using soundings (time-varying pressure, temperature, ozone and humidity profiles along the altitude) from ERA5. This is done in all models except MONC, which uses reference profiles above model top and trace gas concentrations based on McClatchey (1972). For the rest of the models, the following trace gas concentration values were used: carbon dioxide 414 ppm, methane 1.879 ppm and nitrous oxide 0.3328 ppm. Surface albedo of 0.06 and surface emissivity of 0.95 were used by all models except MONC which used surface emissivity of 1 which was the default value. Table 1 provides an overview of the LES setup, highlighting the key differences and similarities across the various codes.

2.2. LES Codes

2.2.1. DALES

The Dutch Atmosphere Large Eddy Simulation (Heus et al., 2010) is one of the models used in our study. It has been successfully applied in various climate regions including subtropical oceans (de Roode et al., 2016). At the foundation of the model are the anelastic equations (Lipps & Hemler, 1982) for a set of prognostic variables including the three velocity components u, v, and w; total water specific humidity q_t ; and liquid water potential temperature θ_t , as well as the number concentration and mass concentration of various hydrometeor species. The time integration makes use of a third-order Runge–Kutta scheme. Scalar advection is represented by the centered difference method, which is also applied for the three velocity components. The subgrid-scale transport of heat, moisture, and momentum depends on a prognostic turbulence kinetic energy (TKE) model. For longwave and shortwave radiation, a multi-waveband transfer model is used in combination with a Monte Carlo approach

RAGHUNATHAN ET AL. 6 of 29

Table 1

Comparison of LES Model Setup					
Feature	MicroHH	SAM-UW	SAM-NOAA	MONC	DALES
Nudging	No Nudging	u, v, T, q_v nudged for $z > 5$ km with $\tau = 1$ hr	u, v, T, q_v nudged for $z > 5$ km with $\tau = 1$ hr	No Nudging	u, v, T, q_v nudged for $z > 5$ km with $\tau = 1$ hr
Droplet Number Concentration	400 cm^{-3}	400 cm^{-3}	calculated from Aerosol ^a	400 cm^{-3}	400 cm^{-3}
Galilean Transform	$(U,V) = (-6, -1) \mathrm{m/s}$	$(U,V) = (-6, -1) \mathrm{m/s}$	$(U,V) = (-6, -1) \mathrm{m/s}$	$(U,V) = (-6, -1) \mathrm{m/s}$	$(U,V) = (-6, -1) \mathrm{m/s}$
Time-Integration Scheme	Fourth-order Runge-Kutta	Third-order Adams Bashforth	Third-order Adams Bashforth	Leap-Frog	Third-order Runge-Kutta
Scalar Advection Scheme	Second-order central difference	Second-order central difference	Second-order central difference	Total variation diminishing scheme	Second-order central difference
Subgrid-Scale Turbulence Scheme	Smagorinsky	1.5-order scheme	1.5-order scheme	Smagorinsky	Smagorinsky
Radiation above model top	P, T, q and O ₃ time-height profiles from ERA5	P, T, q and O ₃ time-height profiles from ERA5	P, T, q and O ₃ time-height profiles from ERA5	Reference profiles from McClatchey (1972)	P, T, q and O ₃ time-height profiles from ERA5
Surface emissivity and albedo	0.95 and 0.06	0.95 and 0.06	0.95 and 0.06	1 and 0.06	0.95 and 0.06
Surface Flux Scheme	MOST ^b	MOST	MOST	MOST	MOST

^aAerosol Number initialized at 476 mg⁻¹ in BL and 32 mg⁻¹ in free troposphere. ^bBased on Monin-Obukhov similarity theory.

(Pincus & Stevens, 2009). For warm clouds, DALES uses a double-moment microphysics scheme featuring two hydrometeors; cloud water and rain (Seifert & Beheng, 2006). A more detailed description of the governing equations, numerical aspects, and the subgrid physics packages is found in Heus et al. (2010).

2.2.2. MicroHH

MicroHH (Van Heerwaarden et al., 2017) is a high-resolution computational fluid dynamics code that performs both direct numerical simulations and large eddy simulations of turbulent flows in doubly periodic domains. For this study, the GPU-enabled version of the code is utilized, offering significant speed and energy efficiency improvements over traditional LES codes. MicroHH uses the anelastic approximation to solve the governing equations of conservation of mass, momentum, and energy (Bannon et al., 2006) with a second-order central differencing spatial discretization scheme and a fourth-order Runge-Kutta time integration method on an Arakawa C-grid. Liquid water potential temperature (θ_l) and water vapor mixing ratio (q_l) are carried as thermodynamic variables, and are conserved for adiabatic processes. MicroHH uses a two-moment warm microphysics scheme with cloud water and rain (Seifert & Beheng, 2006). An interactive radiation scheme (Rapid Radiative Transfer Model for GCM Applications) (Mlawer et al., 1997) is used. A buffer layer is used above 7 km height to dampen turbulent fluctuations. This same overall setup was used to perform the sensitivity studies as well.

2.2.3. MONC

The Met Office/NERC cloud model (MONC, N. Brown et al., 2015) was developed as the successor to the Met Office Large Eddy Model. Here, we used a special version of MONC that is based on revision r10514, but has the capacity to read Lagtraj input. MONC uses an anelastic dynamical core with potential temperature and mixing ratios of water vapor and hydrometeors as prognostic variables and an Arakawa C-grid. Subgrid mixing is done using a Smagorinsky scheme, where the constants follow the "conventional" model of A. R. Brown et al. (1994). For these simulations, we use the SOCRATES radiation scheme (Edwards & Slingo, 1996) and the CASIM twomoment microphysics scheme (Field et al., 2023), revision10387. No ice microphysics was included. For advection of momentum the second-order scheme of Piacsek and Williams (1970) was used, for scalar quantities we used the total variation diminishing scheme of Leonard et al. (1993). MONC uses a leap-frog time integration with an Asselin filter (Asselin, 1972). A weak damping close to the topmost vertical level is applied.

RAGHUNATHAN ET AL. 7 of 29

2.2.4. SAM (University of Washington)

The System for Atmospheric Modeling (Khairoutdinov & Randall, 2003) is an anelastic model with a second-order finite difference discretization of momentum and finite volume representation of scalars (in these simulations: liquid-water static energy; the mass mixing ratios of water vapor, cloud liquid and rain; and the number mixing ratio of rain). Time integration of momentum uses a third-order Adams-Bashforth method, while scalar advection uses a forward-in-time discretization, with the method of Yamaguchi et al. (2011) used here. Subgrid-scale stresses and fluxes are computed using the 1.5-order scheme described in the appendix of Khairoutdinov and Randall (2003). These simulations employ version 6.10.9 of SAM, with the formation, sedimentation and evaporation of cloud droplets and rain represented using the Morrison microphysics (Morrison et al., 2005) with only warm cloud processes. Radiative heating is computed using the Rapid Radiative Transfer Model for GCM Applications (RRTMG, Mlawer et al., 1997). Surface fluxes are computed using the COARE algorithm (Fairall et al., 2003), version 3.6.

2.2.5. SAM (NOAA)

SAM-NOAA is the System for Atmospheric Modeling (SAM; Khairoutdinov & Randall, 2003), version 6.10.10. with a two-moment bin-emulating cloud microphysics scheme (Feingold et al., 1998; Wang & Feingold, 2009; Yamaguchi et al., 2017). This scheme computes prognostically both the mass and number of hydrometeors, and modifies the aerosol size distribution through cloud processes. Aerosol particles are activated based on the computed supersaturation and are then removed from the interstitial aerosol population, increasing the hydrometeor count correspondingly. The process of collision-coalescence decreases both the hydrometeor and aerosol numbers equivalently. During evaporation, each evaporating hydrometeor releases one aerosol particle. Surface precipitation removes hydrometeors from the atmosphere and reduces the aerosol number by the same amount.

The cloud and rainwater modes are described as lognormal distributions with a fixed geometric standard deviation of 1.2. The particle radius threshold differentiating these modes is $25 \mu m$. Condensation and evaporation are computed analytically. Sedimentation of mass and number mixing ratios is determined using mass- and number-weighted average sedimentation velocities for each hydrometeor mode. Hydrometeor breakup is not calculated. Advection is applied to the total mass mixing ratio (total of vapor and condensate mass) and the total number concentration (total of aerosol and hydrometeor number). The water vapor mixing ratio and aerosol number concentration are then calculated as diagnostic quantities of the cloud microphysics scheme. This implicitly maintains the budget of mass and number through condensation, evaporation, collection, and regeneration of aerosol. Further details on this implementation are given in Yamaguchi et al. (2019).

SAM-NOAA calculates the cloud drop number interactively from the aerosol number, and both co-evolve over the course of the simulation due to cloud processing. The aerosol size distribution is represented with a single lognormal mode with a geometric-mean diameter $D_g=128$ nm and a geometric standard deviation $\sigma=1.71$. These parameters were constructed by Narenpitak et al. (2021) from the accumulation mode observed in shipboard measurements during the Atlantic Tradewind Ocean-Atmosphere Mesoscale Interaction Campaign (ATOMIC) field campaign (Quinn et al., 2021). The aerosol number is initialized with 476 mg⁻¹ (number of particles per mg of air) in the boundary layer. This produces at the beginning of the simulation approximately a cloud drop number of 400 cm⁻³ at cloud base. Specifying the initial aerosol number in mg-1 reflects a well-mixed boundary layer and a well-mixed free troposphere, which are reasonable assumptions. The specific value of 476 mg⁻¹ was chosen to approximately obtain at the outset of the simulations, as cloud base, the value of 400 cm⁻³ used by the other models. SAM-NOAA cannot prescribe the cloud drop number when using the Feingold cloud microphysics. Above the inversion, the aerosol number is initialized with 32 mg⁻¹, following Narenpitak et al. (2021). At the initial time, the inversion, identified by the maximum of $\frac{d\theta_l}{dz}$ was located at an altitude of 1,120 m. The aerosol composition was assumed as ammonium sulfate.

Surface fluxes of heat, moisture, and momentum are calculated interactively based on Monin-Obukhov similarity (Monin & Obukhov, 1954). No surface aerosol source is used. Radiation is calculated every 10 s from temperature, gas phase constituents, and liquid water mass mixing ratio and liquid water effective radius, using the Rapid Radiative Transfer Model (RRTMG, Iacono et al. (2008); Mlawer et al. (1997)).

RAGHUNATHAN ET AL. 8 of 29

2.3. Cloud Structure Analysis

2.3.1. Maximum Cloud Length and Organization Index

In order to calculate the largest cloud length at each time step of simulation, the total area covered by the largest cloud in the domain is determined by identifying the maximum number of consecutive adjacent grids based on 4-connectivity (grids in the east, west, north, and south directions) that meet the condition Cloud LWP $(q_l) > 0.01 \text{ kg/m}^2$, denoted subsequently as N_{max} . The cloud length is then defined simply as

$$L_{\text{max}} = \sqrt{A_{\text{max}}},\tag{1}$$

where $A_{\text{max}} = N_{\text{max}} \Delta x \Delta y$ is the maximum area at each time step.

2.3.2. Fractal Dimension

Another way to describe the structure of clouds is to calculate fractal dimension, which is a complexity measure that characterizes the degree of self-similarity in cloud field features. To estimate the fractal dimension, we use the box-counting algorithm (Walsh & Watterson, 1993) whereby the LWP is examined at various resolutions. The field is covered with a box of varying size r, and for each box size the number of non-empty grid boxes N(r) are counted. The fractal dimension D is estimated by linear regression over a log-log plot of box size versus box count, according to the following equation:

$$D = \lim_{r \to 0} \frac{\log(N(r))}{\log(1/r)} \tag{2}$$

where N(r) is the number of boxes occupied by the cloud structures, and r is the size of each box. Fractal dimension quantifies the rate at which an object's geometrical details develop at increasingly fine scales.

3. Results From Model Inter-Comparison

3.1. Overview of the Cloud and Thermodynamic Properties

The results from the multi-model LES ensemble were indicative of a broad agreement among different LES codes when comparing the thermodynamic properties. During the first 48 hr of the simulation, prior to the observation of any kind of convective aggregation, the surface wind speed (Figure 3a), sensible (Figure 3b) and latent heat fluxes (Figure 3c) remain relatively small as the trajectory gradually moves westward and southward, carried by the trade winds. This results in minimal cloud activity, which is evident as low Liquid Water Path (LWP) (Figure 4a), reduced cloud cover (Figure 4b), and a shallow cloud layer (Figure 3d). However, as the trajectory moves southward past the 15° N latitude, we start to see rapid changes in large-scale conditions such as sea surface temperature (Figure 1b) and surface wind speeds (Figure 3a). At the same time, large-scale vertical velocity (Figure 1c) shifts direction, becoming upwards around 10 UTC, aiding strong updrafts and encouraging the boundary layer to deepen. This timing coincides with a continued increase in surface fluxes, a rise in LWP, greater cloud cover, and the deepening of the cloud layer. While surface fluxes and wind speeds peak at ~12 UTC, cloud LWP and cloud depth peak later as substantial surface precipitation or cold pool activity begins in most models (Figures 4c and 4f), after which further deepening of the cloud layer is halted and LWP reaches its maximum. This is likely due to the precipitation depleting the accumulated cloud liquid water, along with the reduction in surface fluxes and increasingly downward large-scale velocity inhibiting the formation of strong updrafts. As surface fluxes and LWP continue to fall, cloud top height reduces or even completely collapses in some models. However, as the trajectory moves further west, we witness this entire process repeating, with the cloud tops in some models returning to their original height before collapsing again.

While these features were common across different models, there were notable differences. For example, in MicroHH, the rise in LWP starts earliest, with precipitation beginning by 08 UTC when cloud tops are still around 1.75 km. In contrast, both SAM-UW and SAM-NOAA lag behind MicroHH in terms of LWP increase by about 4 hr but quickly reach their peak simultaneously with MicroHH. Precipitation in SAM-UW starts simultaneously with MicroHH, whereas SAM-NOAA generates considerably less surface precipitation, which also starts at least 2 hours later. Compared to the other models, SAM-NOAA produced the largest LWP and cold pool fraction but

RAGHUNATHAN ET AL. 9 of 29

19422466, 2025, 10, Downloaded from https://agupubs.onlinelibrary.wiley.com/doi/10.1029/2024MS004864 by NICE, National Institute for Health and Care Excellence, Wiley Online Library on [13/10/2025]. See the Terms and Conditions (https://onlinelibrary.wiley.com/doi/10.1029/2024MS004864 by NICE, National Institute for Health and Care Excellence, Wiley Online Library on [13/10/2025]. See the Terms and Conditions (https://onlinelibrary.wiley.com/doi/10.1029/2024MS004864 by NICE, National Institute for Health and Care Excellence, Wiley Online Library on [13/10/2025]. See the Terms and Conditions (https://onlinelibrary.wiley.com/doi/10.1029/2024MS004864 by NICE, National Institute for Health and Care Excellence, Wiley Online Library on [13/10/2025]. See the Terms and Conditions (https://onlinelibrary.wiley.com/doi/10.1029/2024MS004864 by NICE, National Institute for Health and Care Excellence, Wiley Online Library on [13/10/2025]. See the Terms and Conditions (https://onlinelibrary.wiley.com/doi/10.1029/2024MS004864 by NICE, National Institute for Health and Care Excellence, Wiley Online Library on [13/10/2025]. See the Terms and Conditions (https://onlinelibrary.wiley.com/doi/10.1029/2024MS004864 by NICE, National Institute for Health and Care Excellence, Wiley Online Library on [13/10/2025]. See the Terms and Conditions (https://onlinelibrary.wiley.com/doi/10.1029/2024MS004864 by NICE, National Institute for Health and Care Excellence, Wiley Online Library on [13/10/2025]. See the Terms and Conditions (https://onlinelibrary.wiley.com/doi/10.1029/2024MS004864 by NICE, National Institute for Health and Care Excellence, Wiley Online Library on [13/10/2025]. See the Terms and Conditions (https://onlinelibrary.wiley.com/doi/10.1029/2024MS004864 by NICE, National Institute for Health and Care Excellence, Wiley Online Library on [13/10/2025]. See the Terms and Conditions (https://onlinelibrary.wiley.com/doi/10.1029/2024MS004864 by NICE, National Institute for Health and Care Excellence, Wiley Online Institute for Health a

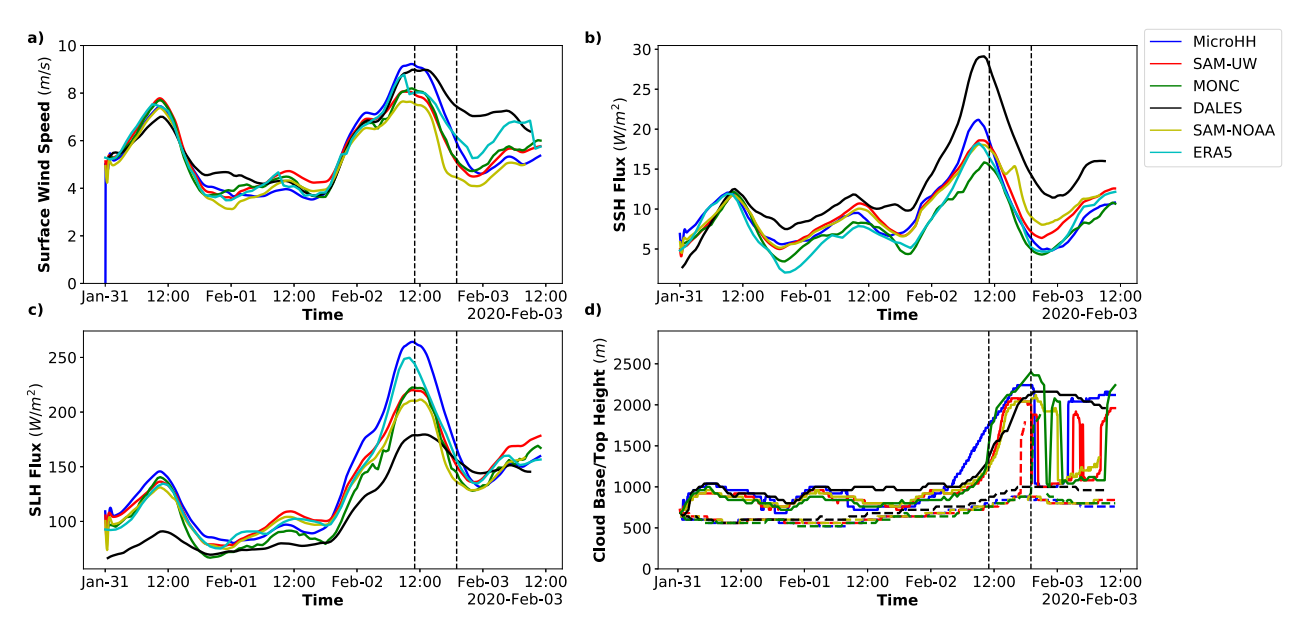


Figure 3. (a) Surface wind speed calculated at first model level (10 m). (b) Surface sensible heat flux and, (c) Surface latent heat flux, (d) Cloud base (dashed lines) and cloud top height (solid lines) as determined from the vertical profile of cloud fraction, with cloud base being the lowest point where cloud cover exceeds 1% and cloud top height being the first level where cloud fraction reaches below 50% of its maximum value. The dashed black lines indicate average time among LES simulations when the maximum cloud size is more than 10 km.

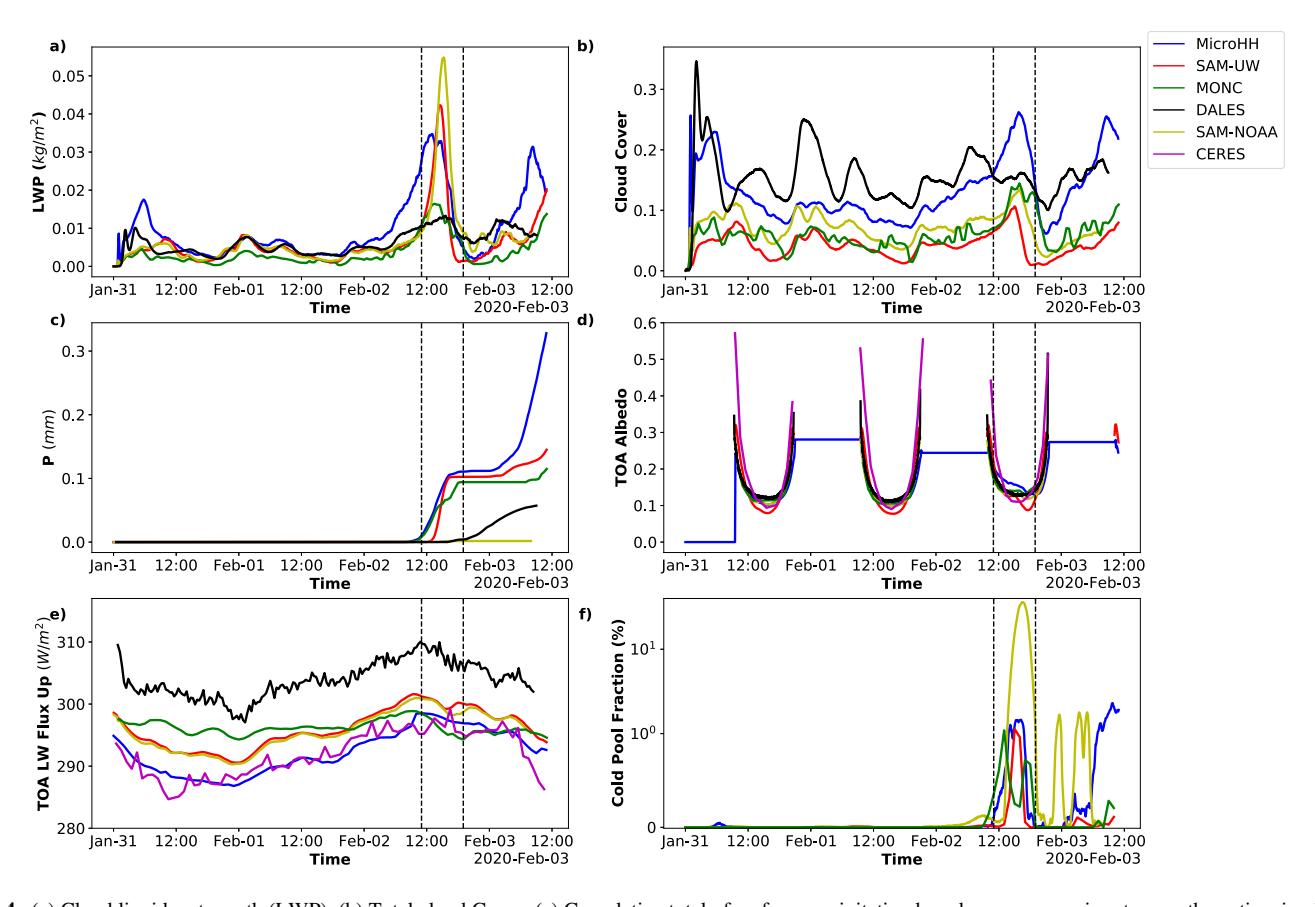


Figure 4. (a) Cloud liquid water path (LWP), (b) Total cloud Cover, (c) Cumulative total of surface precipitation based on average rain rate over the entire simulation domain, (d) Albedo at top of the atmosphere, (e) Upwards long Wave radiation flux calculated at the top of atmosphere, (f) Cold pool fraction measured as fraction of area where mixed-layer height (calculated based on definition for mixed-layer height in Touzé-Peiffer et al. (2022)) is less than 400 m. Axis in y direction here is linear between 0% and 1% and logarithmic above it. The dashed black lines indicate average time among LES simulations when the maximum cloud size is more than 10 km.

RAGHUNATHAN ET AL. 10 of 29

from https://agupubs.onlinelibrary.wiley.com/doi/10.1029/2024MS004864 by NICE, National Institute for Health and Care Excellence, Wiley Online Library on [13/10/2025]. See the Terms

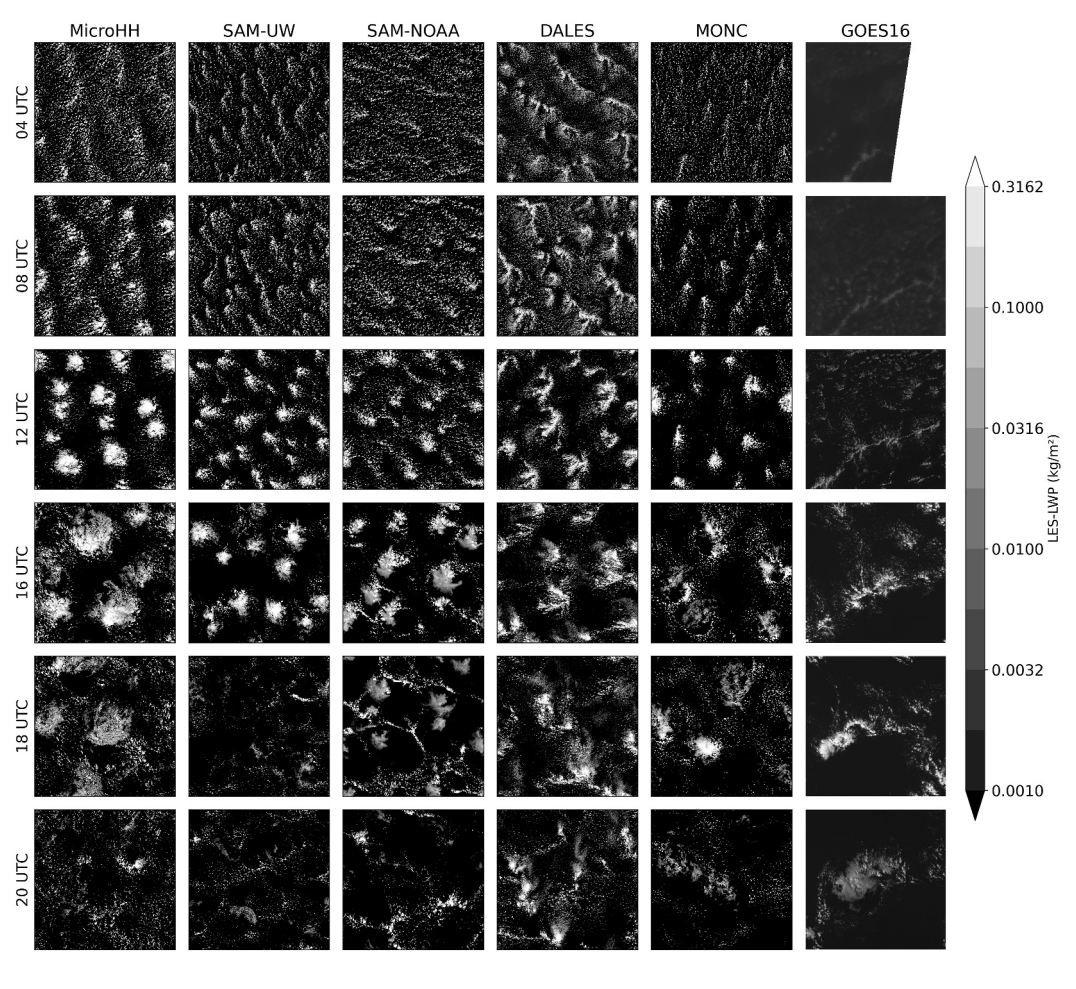


Figure 5. 2D cloud Liquid Water Path with logarithmic scale colorbar (displayed commonly on the right side of the figure) for different models on February 2nd along with extracted GOES-16 satellite image, with $1.6^{\circ} \times 1.6^{\circ}$ grid centered at the same location as LES, covering the same time period as Figure 2 during which transition to Flower was observed. The GOES-16 satellite images use a similar colormap as described in Figure 2.

the smallest accumulated precipitation. The low surface precipitation and large cold pool fraction in SAM-NOAA are consistent with the two-moment bin-emulating cloud microphysics scheme in SAM-NOAA overestimating sub-cloud rain evaporation (Kazil et al., 2021). MONC, on the other hand, produces precipitation at the same time as MicroHH despite having very low LWP values and just as the average cloud top height is seen to rapidly increase. As a result, MONC's cold pool fraction reaches its peak earliest among the models. DALES, in contrast to the rest of the models, only begins to precipitate around 18 UTC when cloud tops reach about 2 km, after the first LWP peak, which continues leading up to the second LWP peak. Additionally, DALES shows larger surface sensible heat fluxes and smaller surface latent heat fluxes compared to other models on February 2nd.

3.2. Comparison With Field Observations

Figure 5 shows the 2D cross-sections of Cloud Liquid Water Path (integrated along z) for the February 2nd case with a log-scale colorbar for better interpretability and resemblance to reflectivity. The corresponding GOES16 satellite images shown at the mentioned times were those of GOES16 visible Band-2 (Red—0.64 µm) images during the day-time and that of GOES16 IR Band-13 (Clean Longwave—10.3 µm) images during night-time. The satellite images were extracted using EUREC⁴A movies github repository (Fildier et al., 2021) as a $1.6^{\circ} * 1.6^{\circ}$ box (which is approximately 176 * 176 km) surrounding the latitude and longitude location of the Lagrangian trajectory during those corresponding times. Although not a strictly like-for-like comparison due to the lack of directly comparable variables, this figure still provides a useful basis for comparison with observations, with

RAGHUNATHAN ET AL. 11 of 29



Journal of Advances in Modeling Earth Systems

10.1029/2024MS004864

LWP > 0.01 kg/m² threshold (mostly light gray and white contours in LES output) used in later analyses to define cloud boundaries.

Initially, at 04 UTC, we see widely dispersed and unorganized clouds resembling a Sugar-type cloud organization. By 08 UTC, cloud patches start to form, with some simulations displaying clouds concentrated along a straight line which somewhat resembles cloud street like structures observed in corresponding satellite images with, however, here marked differences in structure and orientation compared to the satellite images. Also, it is interesting to note that by this point some of the simulations (MicroHH and DALES) are at a more advanced stage of organization compared to others. Despite these early differences, around 12 UTC, small, somewhat organized clouds begin clustering together, evolving into well-defined circular patches, while the surrounding regions become increasingly devoid of clouds. At this time, all the simulations display Flower-type organization. These circular patches continue to grow and persist until 16 UTC, before dissipating in most simulations by 20 UTC.

In comparison, GOES-16 satellite images do not show signs of clustering until at least 16 UTC with well-defined Flowers not evident until at 20 UTC. Despite the similarity in the appearance of the final Flower state between the observation and LES, the delayed appearance of Flowers in observations (not visible until 18 UTC) along with differences in the orientation of cloud streets before cloud clusters form (at 04, 08 and 12 UTC) and eventual length scale of evolved Flower (discussed in Section 3.3), suggests significant differences in cloud evolution between observations and LES. For instance, observations lack the multiple well-defined circular cloud patches (seen among all LES simulations) that in LES initially appear small and later grow into larger cloud clusters. Instead, we see a single cloud street develop directly into a larger cloud cluster by 20 UTC which is also significantly larger in length scale (≈55 km) compared to LES (≈30 km). The fact that multiple LES codes unanimously show this difference in comparison with observations suggests a certain influence of ERA5 largescale forcings along the trajectory which triggers this earlier than observed Flowers. This could also be a result of some underlying process which is not represented among different LES models. For instance, looking at the observations over the entire region instead of just the lagrangian box (Figure 2), we see that the smaller Flowers in the surrounding dissipate earlier, resembling the output from LES, while the Flower within the lagrangian box becomes larger. Considering a broader simulation domain, cloud patches are known to appear much earlier in the day than along our Lagrangian trajectory, as soon as 06 UTC (Saffin et al., 2023). The difference in timings between simulations and observations, also seen in Narenpitak et al. (2021) whose simulated cloud patches were not visible until 00 UTC on February 3rd, may also be related to spinup time in simulations (Saffin et al., 2023), and this issue will be further explored in Section 4.

One possible reason for this difference in cloud evolution appears when comparing the vertical profiles from simulation outputs with the radiosonde data from the Ronald H. Brown vessel, stationed at 13.9°N, 54.5°W, during the day (Figure 6). Although the simulation trajectory reaches the vessel's location only around 17 UTC on February 2nd, comparisons are made for earlier times as well, since Figure 2 shows very little variability in cloud structures between the two regions. It is important to note that the figure compares domain-mean vertical profiles from the LES with radiosonde data from a single location, which may only provide an approximate representation of the broader region's conditions. While the vertical profiles show some broad similarities, notable differences between the radiosonde and LES outputs likely contribute to the observed variations in cloud evolution. For instance, the potential temperature (θ) profiles from multiple radiosondes show a second inversion around 2.5 km with a corresponding gradual increase in boundary layer depth. The timing of cloud cluster formation in satellite images coincides with this height approaching the initially observed second inversion. However, this second inversion is absent in LES. Second, the approximate boundary layer depth estimates from mixing-ratio profiles indicate that observations show a shallower boundary layer than simulations, with its growth lagging behind LES by a few hours. This accelerated boundary layer growth in LES may cause outflow conditions to develop earlier, leading to premature Flower formation compared to observations. Besides this, LES simulations also show lower mixing-ratio values in the lower boundary layer, particularly evident in the 12 and 17 UTC comparisons. Differences we see in wind speed and direction profiles across LES codes further explain the variations in cloud peak positioning and the associated contrails, especially during the early part of the day before cloud clusters form. ERA5 potential temperature profile on the other hand depicts this observed shallower boundary layer during early hours along with the presence of a strong inversion above 1.5 km which is similar to the first inversion noted in observations. However, it still fails to capture the second inversion noted in the observations.

RAGHUNATHAN ET AL. 12 of 29

from https://agupubs.onlinelibrary.wiley.com/doi/10.1029/2024MS004864 by NICE, Nati-

Institute for Health and Care Excellence, Wiley Online Library on [13/10/2025]. See the Term

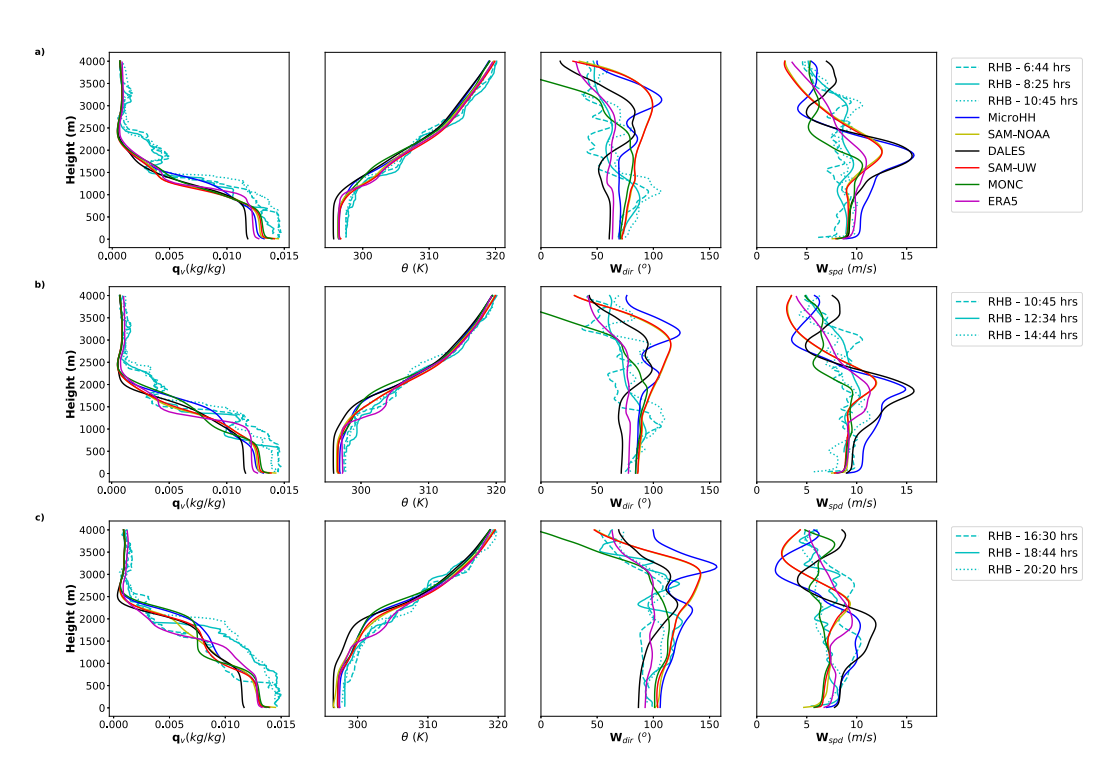


Figure 6. Water vapor mixing ratio, Potential temperature, horizontal wind direction and wind speed (from left to right) along the vertical compared between different model simulation outputs at (a) 08, (b) 12, and (c) 17 UTC on February 2nd, alongside ERA5 profiles at the same times and radiosonde measurements from the RHB vessel. The Lagrangian trajectory is centered at (a) 14.35° N, 51.9° W, (b) 13.95° N, 53.1° W, and (c) 13.9° N, 54.5° W, which is also the location of the RHB vessel.

3.3. Cloud Structure of Flower

What defines a Flower? Traditionally, observational studies (Rasp et al., 2020; Schulz et al., 2021; Stevens et al., 2020) have identified Flowers as large cloudy patches in satellite images. Given their anvil-like vertical structure, what we usually observe as cloudy patches would just be the expanded cloud top region. On the other hand, we also notice peaks in cloud liquid water content among simulations, that occur concurrently as the cloudy patches appear in satellite images (Dauhut et al., 2023; Narenpitak et al., 2021; Saffin et al., 2023). Does the timing of this peak accurately reflect the timing at which the cloud patches reach their largest length scale (i.e., when the area of a single Flower cloud is at its largest)? To explore this, we first analyze the averaged vertical profiles of cloud liquid water content, rainwater content, and average cloud cover (averaged over the x and y dimensions) (Figure 7).

Initially, at 08 UTC, the liquid water mixing ratio, q_l (kg kg⁻¹), is distributed fairly evenly along the vertical, with cloud top heights reaching between 1.5 and 2 km across the models. As the boundary layer expands, the liquid water mixing ratio accumulates around the cloud top which then gets pushed higher. This process coincides with the emergence of Flower clouds, occurring around 12 UTC (as shown in Figure 5). Satellite observations at the HALO circle show a peak in liquid water mixing ratio just below the cloud tops as trade-wind cumulus clouds grow (Section 4.2: Cui et al. (2023)). Examining the cloud cover reveals that, initially, there is a large accumulation of clouds near the cloud base, contrasting with the observations of cloud liquid water mixing ratio. However, as Flower clouds appear, the cloud cover shifts to a bimodal distribution, with the second mode near the cloud top exhibiting higher values. As this process continues, the largest scale Flower clouds emerge around 16 UTC. At this time, the total liquid water path is reduced from its peak (Figure 4), but the cloud cover near the cloud top reaches its highest value, even with a slight decrease in liquid water mixing ratio in that area, as noted in MicroHH. A larger cloud cover with smaller liquid water mixing ratio is indicative of a larger lateral spread in liquid water mixing ratio along the larger cloud area associated with thin outflow clouds. Additionally, the mode near the cloud base in cloud cover decreases. By 20 UTC, most models indicate the dissipation of the cloud layer, leaving very little cloud cover near both the cloud base and cloud top. The exception to this is DALES which

RAGHUNATHAN ET AL. 13 of 29

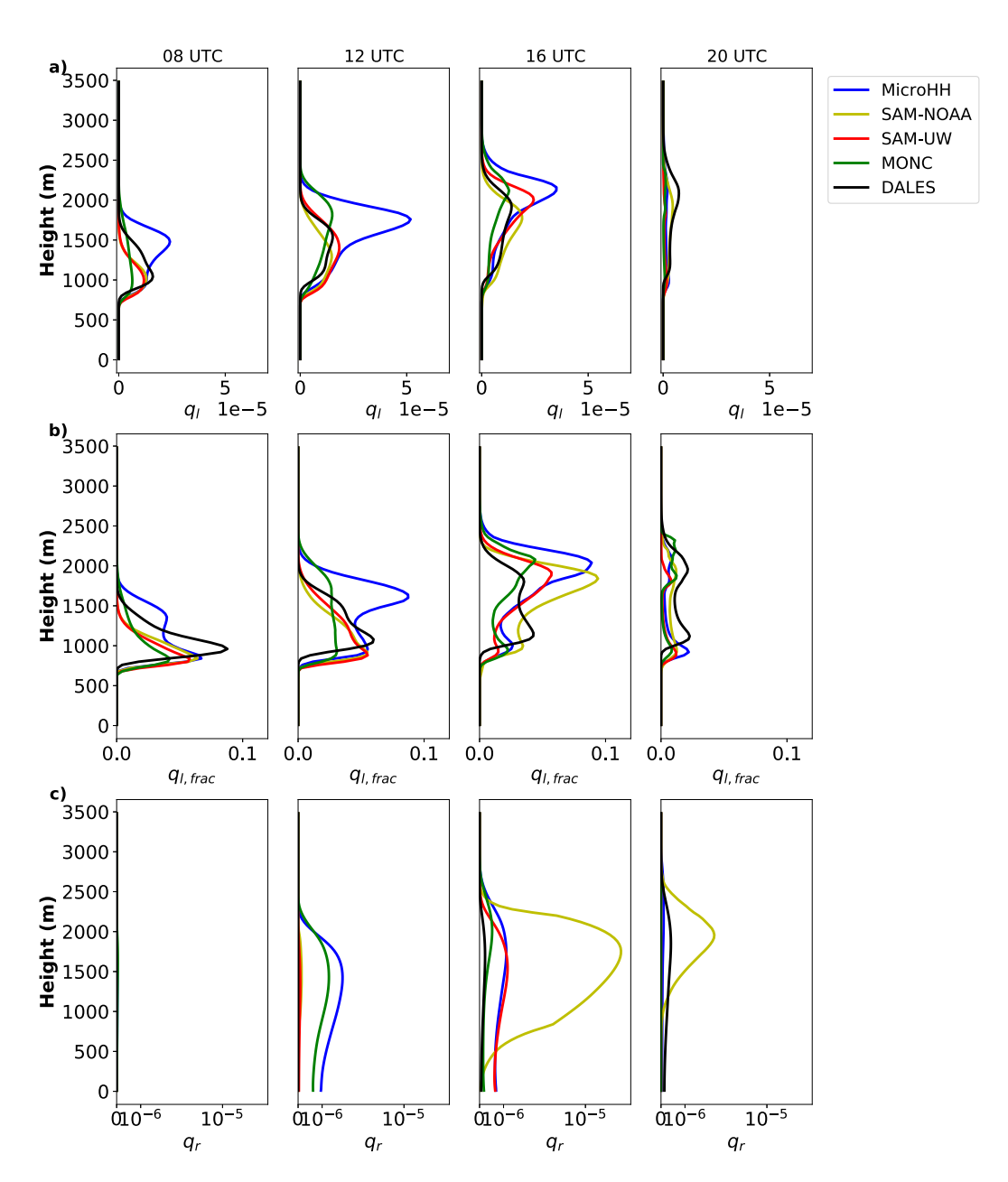


Figure 7. Average (a) Cloud Liquid Water Mixing Ratio q_l (kg/kg) (b) Cloud Fraction (c) Rain Water Mixing Ratio q_r (kg/kg) along the vertical direction on 2nd February 2020 during indicated times (in UTC) for different LES codes.

continues to possess a residual cloud layer close to the cloud top and as witnessed from liquid water path (Figure 5a) and total cloud cover plots (Figure 5b) continues until the appearance of a second peak.

Examining the rainwater mixing ratio $q_r(kg kg^{-1})$ during these times, we note that most of the models begin to produce rain as the cloud tops exceed 2 km height. This then continues until 20 UTC when the cloud layer dissipates. In SAM-NOAA however, we notice that the model produces significantly larger rain compared to rest of the models, which however does not reach the surface suggesting evaporation of most or all of the produced rain within the cloud/sub-cloud layer. The two-moment bin-emulating cloud microphysics scheme in SAM-NOAA has been found to overestimate sub-cloud rain evaporation (Kazil et al., 2021). This may also explain the significantly larger cold pool fraction in the SAM-NOAA simulation compared to the other models (Figure 4i).

RAGHUNATHAN ET AL. 14 of 29

from https://agupubs.onlinelibrary.wiley.com/doi/10.1029/2024MS004864 by NICE, National Institute for Health and Care Excellence, Wiley Online Library on [13/10/2025]. See the Terms

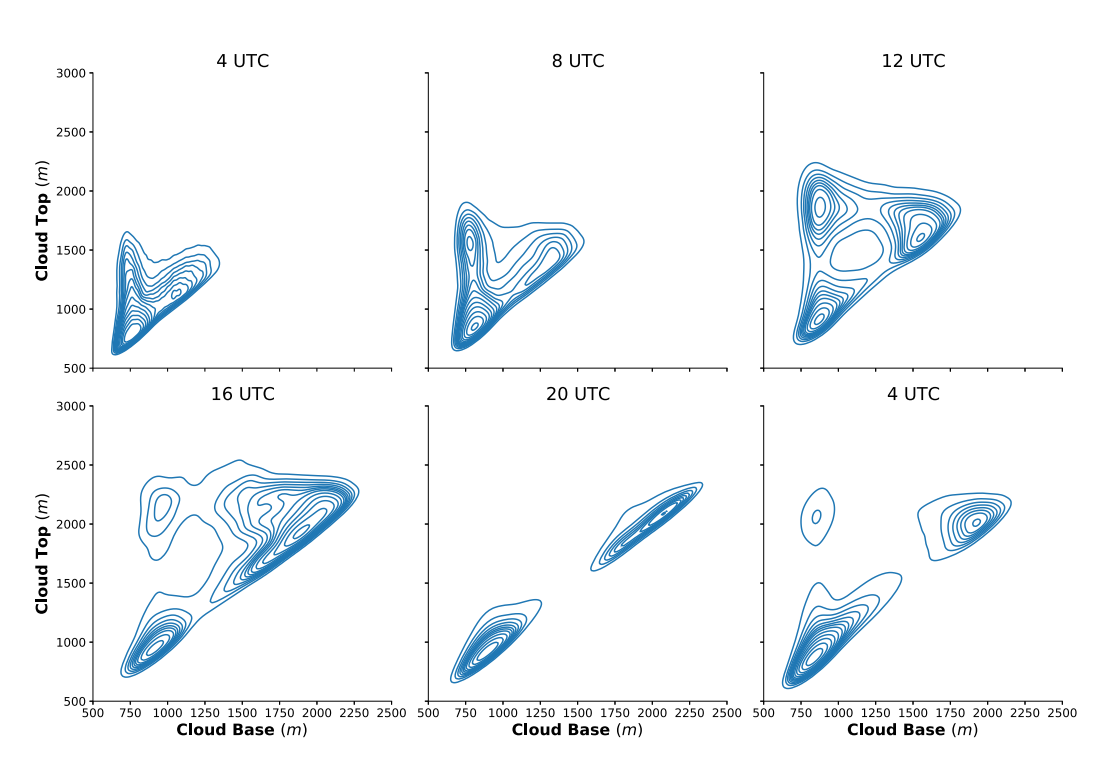


Figure 8. Joint probability density of cloud base and cloud top at specific times, where the cloud top is defined as the highest point and the cloud base as the first point with non-zero cloud liquid water content (according to the MicroHH simulation). The plots begin on February 2nd at 04 UTC (top left) and continue every four hours, including an additional plot at 04 UTC on February 3rd (bottom right).

A similar pattern of events emerges when examining the joint probability density of cloud base and cloud top height over this time period using just the MicroHH simulation (Figure 8). This is done by identifying cloud base and corresponding cloud top heights of each individual column and determining the joint probability density at each displayed time. There are three distinct modes that emerge: columns with both low cloud tops and bases (cloud near the lifting condensation level), columns with high cloud tops and bases (thin, near-inversion cloud), and columns with deeper clouds having high cloud tops and low cloud bases (similar to Figure 2 in Glenn and Krueger (2014) but within shallow cumulus regime), evident even during the early Sugar phase with scattered clouds. The cloud tops begin to rise between 04 and 08 UTC, with columns having deeper clouds and a higher cloud top increasing in number. This increase continues until the appearance of a distinct trimodal distribution by around 12 UTC, with equal proportions of columns in each category. As significant precipitation starts around this time (Figure 4c), deeper and higher clouds begin to dissipate, giving way to anvil-shaped clouds with large, thin cloud bands around the cloud top, sustained by moisture from a few deeper clouds connecting the cloud base to the anvil (evident in Figure 7 by 16 UTC). These clouds are found between 16 and 20 UTC, as the boundary layer continues to grow in height. Somewhere between this time period, the deeper clouds that supply the anvil top are cut off from the base, leading to the gradual dissipation of the anvil top beyond 20 UTC on February 2nd. The suppression of these deeper updrafts is thought to play a significant role in shortening the life span of Flower clouds, potentially due to the change in large-scale subsidence (Figure 1c) occurring around this time and/or increased precipitation and cold pools (seen to occur between 14 and 18 UTC (Figure 4f) that inhibit formation of deep updrafts. Narenpitak et al. (2021) showed that a weak large-scale upward velocity produced smaller Flowers, with shallower boundary layer and reduced precipitation when compared to case with regular large-scale upward velocity, highlighting the importance of large-scale subsidence in modulating Flower time and length scale. In three of our simulations, we observe the rapid reappearance of these deeper clouds by 04 UTC on February 3rd, accompanied by a second peak in LWP, indicative of the reemerging Flower cloud (Figure 4a). This occurs at a much faster rate compared to the initial phase of Flower clouds, as the boundary layer, having already deepened during the first Flower phase, remains in this state until favorable conditions are reestablished.

The findings derived from cloud top and cloud base distributions in LES simulations are reflected in satellite observations (Cui et al., 2023). Initially, only a few cloud patches exhibited heights surpassing 2500 m during the

RAGHUNATHAN ET AL. 15 of 29

onset of Flower development (Figure 6 in Cui et al. (2023)). Nevertheless, as the system advanced towards maturity (12:20–19:00 UTC), substantial sections were found above this level, with many of these clouds situated above the inversion base, which was at a height of around 2800 m (Figure 14 in Cui et al. (2023)). Similar to our simulations, the patches maintained a similar cloud top height, whereas the overall cloud area of the Flower diminished during the decay phase (19:00–21:00 UTC). Although these observations were made around the HALO circle and the overall magnitude of cloud top height observed was slightly larger (Dauhut et al., 2023), the overall process and timing resemble those of our simulations.

As the changing combinations of cloud top and cloud base height shown for MicroHH in Figure 8 likely correspond to different liquid water paths total LWP, including both cloud liquid and rain and might be related to precipitation formation, the evolving distributions of total LWP and precipitation are shown separately for each model in Figures 9a-9e. While shapes of the precipitation and total LWP distributions are similar across models, the timings and amount of precipitation, and of columns with total LWP exceeding 1 kg m⁻³ vary widely. An estimate of cloud cover (based on a total LWP threshold of 10⁻³ kg m⁻²) can be read off from the y-intercept at left, and while most models show cloud cover maximized for 14-18 UTC, the cloud cover in DALES maximizes earlier for 06-10 UTC. The peak total LWP and population of large total LWP (>3 kg m⁻²) tend to peak at 14-18UTC and then decrease afterwards, though DALES peaks during the later 18-22 UTC period. Also shown on each plot is the CDF of accumulated precipitation across the same four time periods. The domain-mean accumulated surface precipitation during each period can be read off on the y-intercept on the right axis, and peaks earliest for MicroHH (10-14 UTC) and latest for DALES (18-22 UTC). Note that the peak cloud cover and accumulated precipitation coincide in only two of the models, SAM-UW and SAM-NOAA. The few columns with total LWPs approaching 10 kg m⁻² contribute less to the accumulated rainfall than the more widespread areas with total LWP between 0.3 and 3 kg m⁻², which account for the majority of surface precipitation. As these values of total LWP are relatively rare, half of the precipitation falls in less than 1% of the domain.

To understand how well models agree in their relationships between total LWP and surface rainrate, Figure 9f shows the mean surface rain rate in each total LWP bin over the full period shown in Figures 9a-9e (06-22 UTC). Three models (MicroHH, SAM-UW and MONC) agree to within roughly a factor of two across a broad range of total LWP (~0.1-10 kg m⁻²), despite using different microphysical schemes (as described in Section 2.2). This relationship should be viewed as specific to the cloud droplet number concentration (400 cm⁻³) that was prescribed in these runs and in DALES, and it would be expected to change with variations in cloud droplet number concentrations, DALES follows a similar relationship between total LWP and precipitation, though smaller by a factor of 2-4. SAM-NOAA, which was the only model to use prognostic aerosol and was shown to have a bias towards low precipitation in Kazil et al. (2021), has precipitation rates one to two orders of magnitude smaller than MicroHH, SAM-UW and MONC for a given total LWP. The large rainwater mixing ratios at 16 and 20 UTC near cloud top in Figure 4 show that rain is being formed in SAM-NOAA but seems to preferentially evaporate (when compared to the other models) before reaching the surface. Such relationships between total LWP and precipitation at a local level seem like a promising way for the microphysics of these high-resolution models to be constrained by observations at their grid scale, as in the joint retrievals of cloud and rain in Lebsock et al. (2011) and Dzambo et al. (2021). It should be noted that the mean precipitation in Figure 9f hides variability in precipitation at a given total LWP depending on other conditions, such as sub-cloud humidity that would affect rain evaporation or shear that might cause precipitation to fall outside the cloud in which it was formed.

We further examine the time series of individual length scales of the Flowers that develop through the day across different models. $N_{\rm max}$. A noticeable difference in timing can be discerned when comparing the LWP (Figure 4a) with the time series of maximum cloud length (Figure 10a) as hypothesized above. However, there is some correspondence with the cloud top versus cloud base distribution, with the growth in Flower length scale peaking just before the deeper clouds are cut off (around 14 UTC). Similarly, we notice growth in Flower length scale associated with a rapidly reemerging anvil cloud top once deeper clouds reappear. A brief comparison with the observed Flower length scale shows that its growth begins around the same time as in the LES, but continues throughout the day, reaching a maximum near 00 UTC on 3 February 2020. Additionally, the observed length scale is significantly larger than that simulated by the LES. Time evolution of organization index I_{org} is shown in Figure 10b. The time of evolution of I_{org} for different models (Figure 10b) show development of organized structures first on early February 1st and again on early February 2nd. However, DALES and MicroHH show presence of organization throughout the simulation with peaks during those times.

RAGHUNATHAN ET AL. 16 of 29

from https://agupubs.onlinelibrary.wiley.com/doi/10.1029/2024MS004864 by NICE, National Institute for Health and Care Excellence, Wiley Online Library on [13/10/2025]. See the Terms

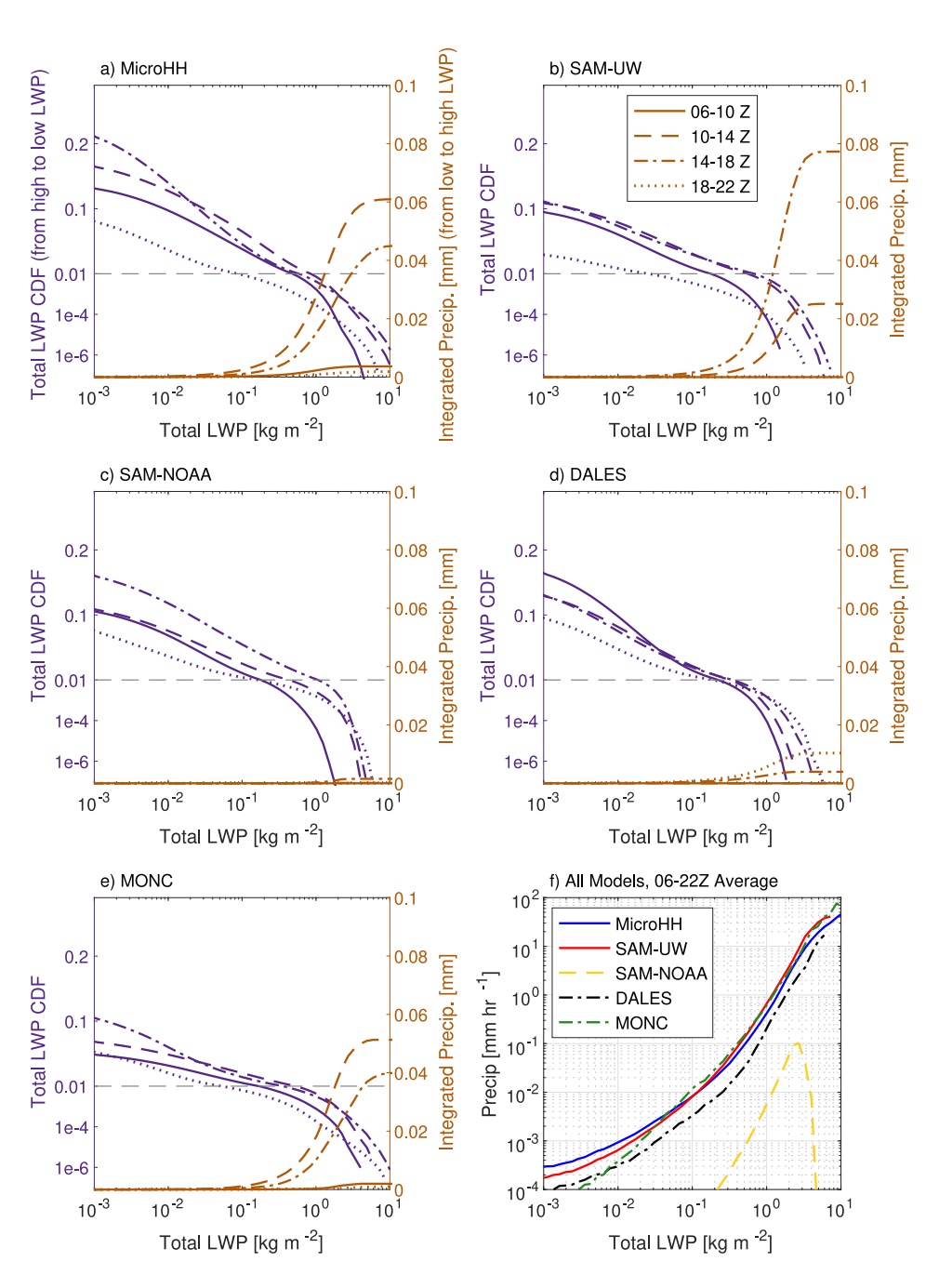


Figure 9. In (a–e), the evolution of cloud and precipitation in each model are shown for four hour time periods surrounding the four times (08, 12, 16, and 20 UTC on 2 February) in Figure 7. The cumulative distribution function (CDF) of total (cloud + rain) liquid water path (LWP), accumulated from high to low values, uses a y-axis (at left) with a linear scale above 0.01 and a logarithmic scale below, following Nugent et al. (2022). Each panel also displays the integrated precipitation over time and for all total LWP up to the value on the x-axis. The right y-axis shows the values of that integrated precipitation, and the domain-mean accumulated precipitation for each period and model can be read off from the y-intercept on the right hand axis. In f), the average precipitation rate for each total LWP bin is shown for the period 06–22 UTC in each model. All quantities shown in this figure are based on total LWP and precipitation values in individual model columns with $\Delta x = \Delta y = 150$ m.

Figure 10c, which shows the time evolution of fractal dimension among different LES codes, shows that the complexity in cloud structure increases with time generally in all models, but shows a sharp decrease with the onset of precipitation. SAM-NOAA and MicroHH can capture finer cloud details and have the most intricate cloud field patterns. While typical fractal dimension values for shallow cumulus clouds range from about 1.35 to

RAGHUNATHAN ET AL. 17 of 29

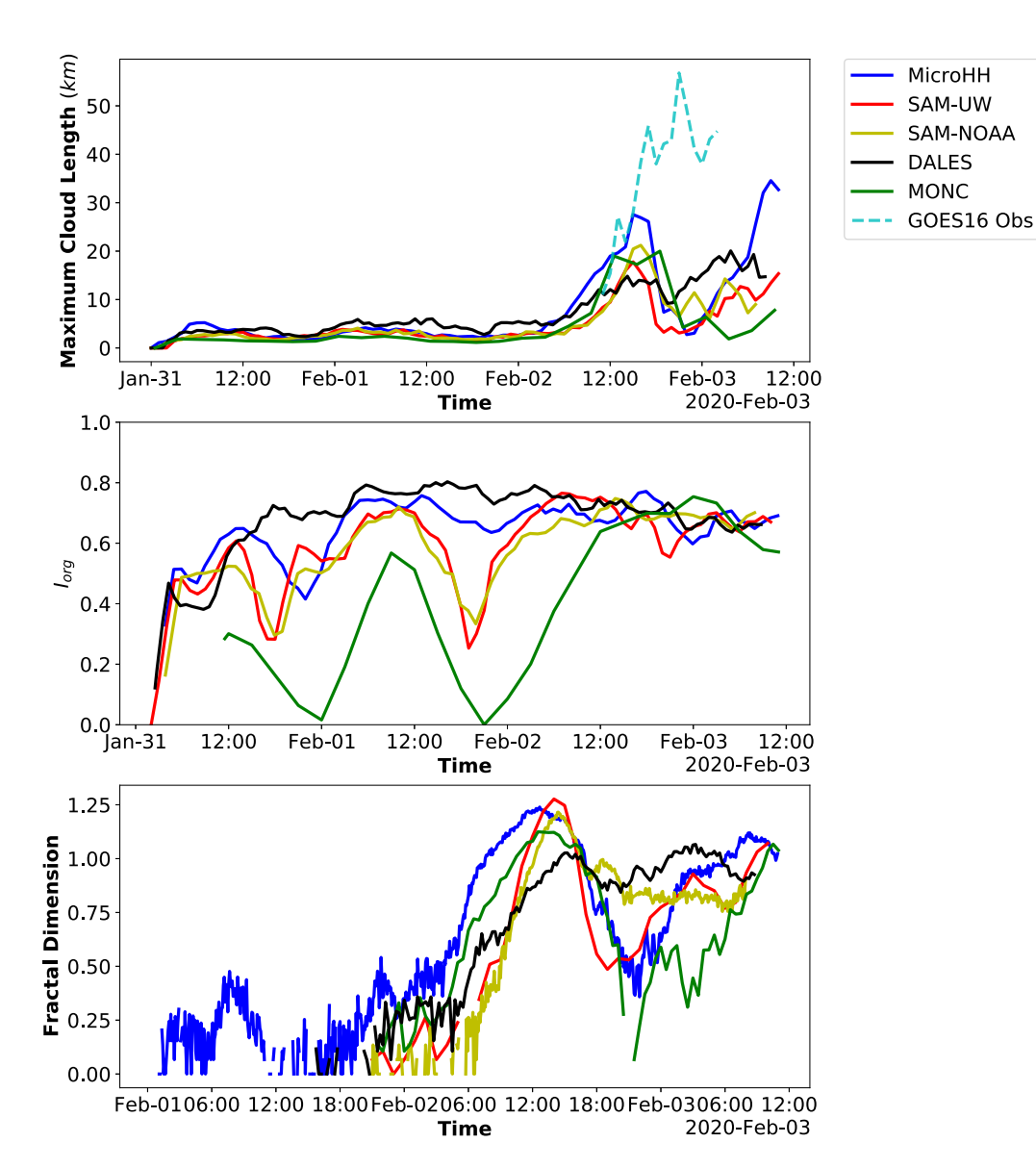


Figure 10. (a) Maximum Cloud Length from LES calculated based on tracking individual clouds as all continuous elements with cloud LWP > $0.01 \, (kg/m^2)$ and from observation using GOES-16 visible and infrared satellite images identifying the largest continuous white pixel areas, following a similar method to that used for the LES output. (b) Organization index I_{org} calculated based on area under Nearest Neighbor Cumulative Distribution Function (NNCDF). NNCDF is derived using smallest distance between the tracked individual clouds. Values of $I_{org} > 0.5$ indicate clustered organization. (c) Fractal dimension calculated based on Equation 2 for different models starting February 1st.

1.55 (Cahalan & Joseph, 1989), the values in our simulations remain much lower, between 0 and 0.5 prior to the emergence of Flower clouds. A likely explanation is that the horizontal grid spacing of 150 m is too coarse to fully capture smaller clouds, which results in underestimated fractal dimensions. As cloud sizes increase around February 2nd, these values start to increase and become more consistent with those reported in earlier studies.

3.4. Temporal Analysis of Thermodynamic Peaks and Cloud Size Distribution

Following our discussion on the timing delay between LWP and Flower length scale peaks, we recognize that multiple factors may influence the cloud clustering observed in satellite images of Flowers. For instance, large surface precipitation rates when combined with cold pools have proved to play a role in suppressing convection within the region of its influence (Drager & van den Heever, 2017). The strong surface winds generated as a result of cold pools (a) enhance surface sensible and latent heat fluxes within the cold pool and (b) induce horizontal

RAGHUNATHAN ET AL. 18 of 29

from https://agupubs.onlinelibrary.wiley.com/doi/10.1029/2024MS004864 by NICE, Nati-

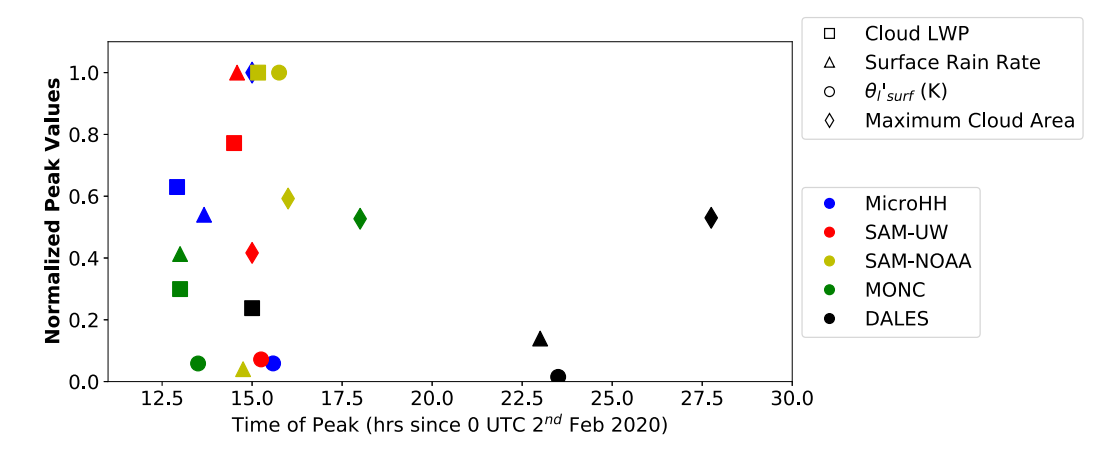


Figure 11. Normalized Peak values of LWP (max = 54.8 g/m^2), Surface Rain Rate (max = 1.187 mm/day), Surface liquid water potential temperature variance (max = 0.72 K^2) and maximum cloud area (max = 759 km^2 which is $\approx 27.55 \text{ km}$ in length) identified to be the highest value from each time series data of corresponding variable between the start of simulation and 00 UTC on February 3rd.

convergence and upward motion along the cold pool boundaries, which can sometimes trigger convective updrafts. Both Vogel et al. (2021b) and Touzé-Peiffer et al. (2022) have identified mesoscale cloud arcs associated with cold pools during February 2nd around the HALO circle following the observance of Flowers. In the previous section, we discussed the presence of a large number of deeper convective updrafts during the developing stage of Flower which then begin to shrink in number concurrently as Flowers start to decay suggesting a causal relationship between the reduced number of deeper updrafts and decay of Flower clouds. Precipitation or even production of rain close to these deeper updrafts could suppress such convection, triggering the decay of Flower by cutting off moisture supply to the thin anvil top. To understand how this sequence of events influences cloud organization in our case, we analyze these individual peaks (LWP, surface rain rate, Cold pools and Flower cloud length scale) to summarize the timing of each process in a single plot.

Figure 11 shows the peaks of four different variables across the models, and each peak is normalized based on the highest value of the variable before 3rd February. (In DALES, the peaks are normalized over the entire simulation rather than capping it to just before 3rd February, because DALES produces Flowers later during early February 3rd compared to rest of the models). For this plot we utilize the variance in surface liquid water potential temperature $\langle \theta'^2 \rangle_{x,y}$ as an indicator of cold pool intensity, as significant local temperature drops in certain areas within the domain would still manifest as large variances in potential temperature. Though no singular pattern emerges, we recognize some consistent behavior across all models. For instance, most of the peaks occur between 12 and 17 UTC. The peaks in liquid water path and surface rain rates consistently precede the peak in largest cloud length across all models. However, peaks in surface rain rate and LWP occur close to each other among some of the models (SAM-NOAA, SAM-UW and MONC) while the LWP peak clearly precedes peak in surface rain rate in others (DALES and MicroHH). The span of peak timings, however, varies significantly across models. In SAM-UW and SAM-NOAA, all of the peaks occur within \sim 1 hr of each other. The greatest variation in timing is between the peaks in LWP and occurrence of largest Flower length scale, which varies from 2.5 to 5 and 12 hr between MicroHH, MONC and DALES, respectively. Cold pool activity, however, shows no such consistent patterns and peaks either before or close to the time when Flowers reach their largest length scale.

Analyzing cloud size distributions provides insights into the variations in cloud structures seen across different models. We use the methodology described in Neggers et al. (2003) to compute cloud size densities, which are effectively characterized by a power law, as shown in observational studies. Identifying the length scales where this scaling breaks down, indicated by a sharp decline in number density beyond a specific cloud length, serves as a useful metric for distinguishing between organized and disorganized states. Figure 12 shows the cloud number density for different models plotted against their corresponding cloud lengths. Cloud number densities during two different time periods separated as period before observation of Flower (first 52 hr of simulation until 04 UTC on February 2nd, solid lines) and the period encompassing different stages of Flower (from 04 UTC on February 2nd to 06 UTC on February 3rd, dot dashed lines) are shown. Marked differences in cloud length scale and its

RAGHUNATHAN ET AL. 19 of 29

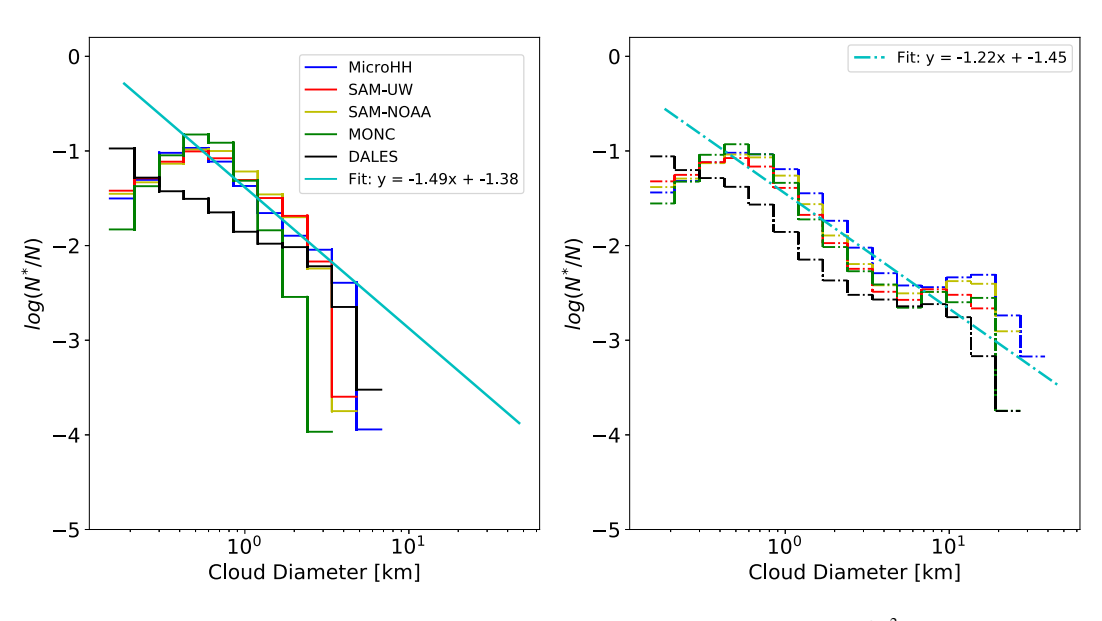


Figure 12. Normalized cloud size density distribution based on cloud liquid water path $> 0.01 \text{ kg/m}^2$ for first 52 hr of February 2nd case till 04 UTC on February 2nd (solid lines) and for 26 hr between 04 UTC on February 2nd and 06 UTC on February 3rd (dashed lines) during which we see Flowers.

distribution can be noted between the two time periods and the overall distribution during both these periods remain fairly consistent among different models. DALES, however, displays smaller cloud densities for clouds with diameter less than 1 km compared to rest of the models. The polynomial fit of the corresponding power law during time periods reflect these differences with the varying slope values (a) of -1.49 and -1.22 during the two periods respectively. The exponent values (-1.49,-1.22) are within the range of values derived in previous observational and LES studies of cumulus clouds (-1.16 for observed fair-weather cumulus clouds over Southern Great Plains (Chandra et al., 2013), -1.9 and -2.3 for LES and aircraft observations of non precipitating cumulus clouds over Houston, TX (Jiang et al., 2008), -1.7 for LES study of cumulus clouds over BOMEX, SCMS and SGP (Neggers et al., 2003)). We also see a scale break occurring for both the smallest and largest length scales. Interestingly, during the Flower phase, the scale break occurs on the other side of the polynomial fit with higher density of clouds with lengths exceeding approximately 5 km compared to what the power law predicts. Neggers et al. (2019) identified a similar growth in larger cloud structures as spatial organization increased in their simulations of the RICO case. They also observed greater variability in small clouds with increasing spatial organization; however, in our case, this effect is minor and confined to the smallest cloud sizes.

4. Flower Formation: Sensitivity Analysis Using a Single Model

To examine how changes in simulation parameters influence the timing, scale, and formation of Flowers, we conducted LES simulations using the MicroHH LES model, altering only the parameters under sensitivity testing while keeping the rest of the simulation setup fixed.

4.1. Cloud Droplet Number Concentration

From discussions in the previous section, we notice that the timing of cloud growth, precipitation initiation and cold pool formation plays a critical role in Flower length and time scales, all of which are influenced by cloud microphysics. In particular, changing the cloud droplet number concentration has been shown to modulate precipitation and thus any subsequent changes in overall mesoscale circulation (Savic-Jovcic & Stevens, 2008; Wang & Feingold, 2009). Thus, in this section we examine what happens to these thermodynamic parameters as this value of fixed cloud droplet number concentration is varied and how they affect the eventual length scale of the formed Flower.

As the Cloud Droplet Number Concentration (CDNC) increases, the peak value of the liquid water path (LWP) also rises and occurs earlier, while the onset of precipitation and cold pool activity are delayed (Figure 13). Simulations with lower CDNC exhibit significantly more precipitation than those with higher CDNC values;

RAGHUNATHAN ET AL. 20 of 29

however, the scenario with the lowest CDNC experiences precipitation much sooner, leading to a larger overall accumulation and an absence of Flower-like cloud features. This suggests that moisture is constantly being removed from the cloud layer as rain, preventing Flower formation despite favorable large-scale environmental conditions (as mentioned in the introduction) when the CDNC is low enough. For cases that exceed a certain threshold (e.g., the 50 cm⁻³ case in Figure 13), there seems to be a positive correlation between peak LWP values and corresponding CDNC values (14a). However, while exploring correlation between the CDNC and rest of the parameters we notice a general inverse linear relationship with the exception of the largest CDNC case which stands out as an anomaly. This is particularly evident when comparing different peaks in cloud length scale of Flower (14d) which show an approximately inverse linear relationship for three intermediate CDNC peaks (50 cm⁻³, 150 cm⁻³, 400 cm⁻³) which breaks down at both the lowest and highest CDNC values. The largest CDNC case (700 cm⁻³) produces the largest Flower cloud with most LWP despite having the lowest surface rain rates and cold pool activity. This finding contradicts Seifert and Heus (2013), which reported a linear trend where higher CDNC values reduced rain rates (consistent with our results) but also decreased organization. In their case study, the organization was primarily driven by cold pools. Another key difference between the largest and intermediate CDNC cases is that, in the largest CDNC case, the onset of precipitation and cold pools is delayed. This delay allows the Flower length scale to expand before precipitation begins, unlike in the other cases. Seifert et al. (2015), in exploring trade wind cumulus response to CDNC variations, found that sufficiently high CDNC inhibits precipitation, allowing clouds to grow deeper. More recently, Alinaghi et al. (2024) in exploring the sensitivity of cloud organization to cloud droplet number concentration through cold pools, identified that for the largest CDNC case in their simulations (1,000 cm⁻³), the cold pools produced were smaller in number and thus were more dispersed than for cases with smaller CDNC values. In such cases with weakened cold pools, convection remains localized in moist regions due to the absence of evaporation-driven downdrafts that typically oppose upward motion under deeper convective clouds, thereby keeping moist areas moist and promoting aggregation (Muller & Bony, 2015). Interestingly, our simulations showed that the delay in precipitation timing did not consistently align with an increase in CDNC. In fact, except for the case with the highest CDNC, precipitation occurred at approximately the same time, despite a steady decrease in precipitation rates. Apart from this, the overall trend of increased LWP, decreased rain rates and thus decreased cold pool activity with increased CDNC matches the finding from Alinaghi et al. (2024) (Figure 14).

4.2. Simulation Lead Time

LES models need an adequate spin-up period to develop turbulent eddies and remove biases from the initial conditions. For simulating disorganized shallow cumulus cloud fields, this typically requires only a few hours. However, a larger spin-up time may be required when simulating mesoscale organization especially with transitions between organized states. This is largely intended to provide enough time for mesoscale moisture to converge within the simulation domain, which is considered essential for triggering mesoscale organization. In our control simulation, we started off at 00 UTC on January 31st, which is more than 48 hr before the day of interest. Saffin et al. (2023) found that their kilometer-scale, Eulerian simulations produced smaller cloud structure and weaker mesoscale organization when initialized 24 hr later than the original simulation. In our study (Figure 15), we observe a similar outcome: the simulation initialized 1 day later (at 00 UTC on February 1st) produces smaller-scale Flowers compared to the control case and another simulation initialized 1 day earlier (at 00 UTC on January 30th). Both of these simulations, with a lead time of more than 48 hr, generate similar time series profiles for LWP, precipitation, and Flower length scale.

To quantify moisture convergence in the domain, we examine the spectra of the column-integrated total water mixing ratio (precipitable water PW) over time, plotting the length scale which captures two-thirds of its variance (Figure 15d). This length scale is calculated following the method in de Roode et al. (2004). In the lead-up to the observed day of Flower clouds, the two simulations with lead times over 48 hr exhibit nearly identical length scales, with a gradual increase beginning in the middle of January 31st. By contrast, the simulation initialized at 00 UTC on February 1 shows a significantly smaller length scale compared to the other two simulations by midday. This is followed by a steady growth in length scale, which only reaches values comparable to the other two simulations by February 3. This insufficiency in scale of moisture convergence by the time favorable large-scale conditions are met explains the relatively smaller length-scale of Flower clouds for the simulation with smaller lead time.

RAGHUNATHAN ET AL. 21 of 29

10 cm⁻³ 50 cm⁻³

150 cm⁻³ 400 cm⁻³

 $700 \ cm^{-3}$

19422466, 2025, 10, Downloaded from https://@pupubs.onlinelitrary.wieje.com/do/10.10929024MS004864 by NICE, National Institute for Health and Care Excellence, Wiley Online Library on [13/10/025]. See the Terms and Conditions (https://onlinelibrary.wiley.com/terms/

are governed by the applicable Crea

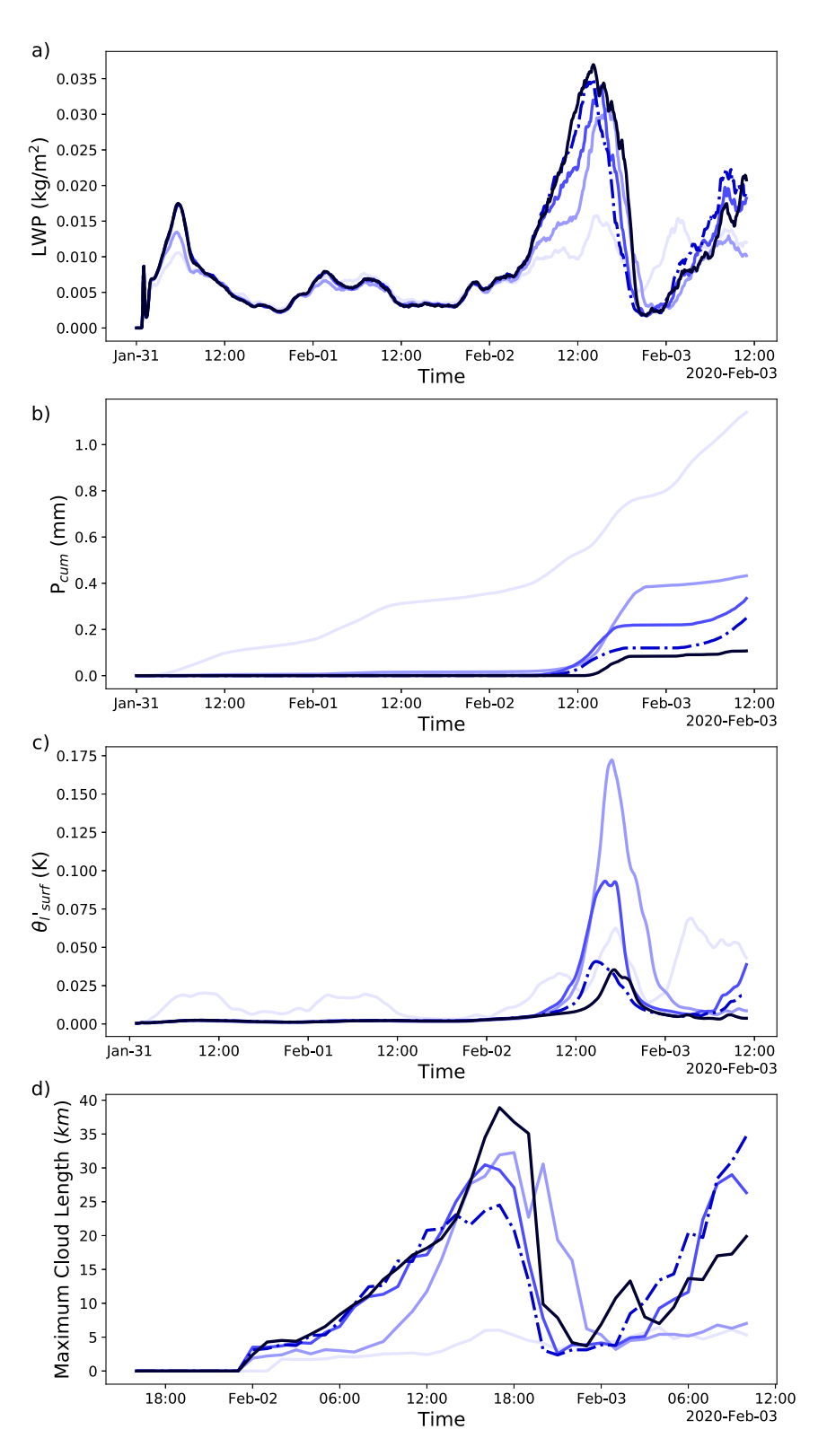


Figure 13. (a) Cloud liquid water path (b) Cumulative total of Surface Precipitation based on average rain rate over the entire simulation domain, (c) Variance in liquid water potential temperature at first model level indicative of any strong cold pools within the domain, (d) maximum cloud length derived from tracked individual cloud structures based on 2d liquid water path fields with LWP > 0.01 for MicroHH simulations with varying cloud droplet number concentrations. The dashed lines here indicate the simulation which was used in the inter-comparison.

RAGHUNATHAN ET AL. 22 of 29

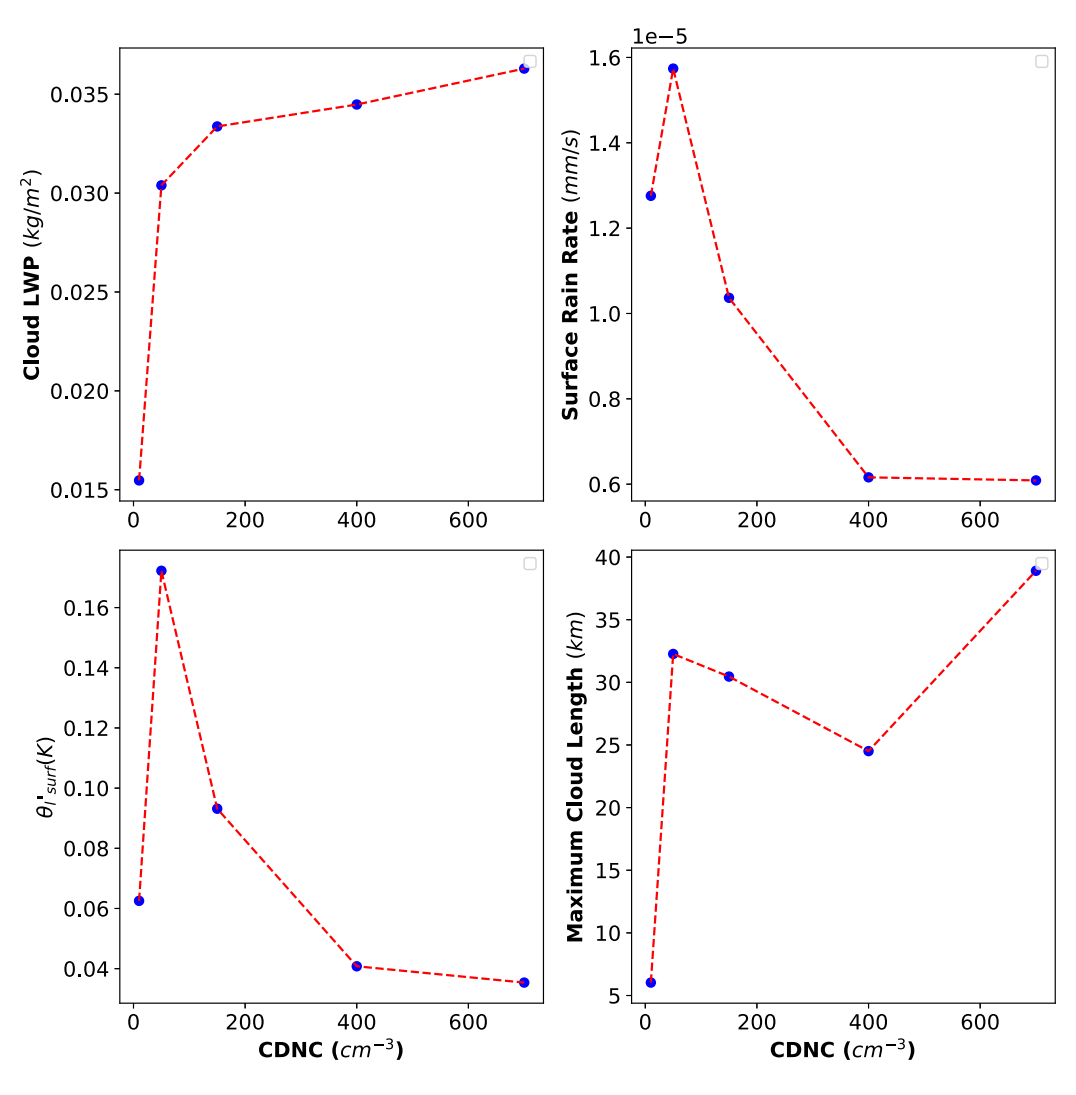


Figure 14. Values of peaks from Figure 13 against corresponding Cloud Droplet Number concentration values.

4.3. Ensemble Runs

Similar to the impact of simulation lead time, variations in the initial randomization of fields can lead to localized differences that evolve over time, potentially affecting the cloud structures that develop during the simulation of organization. This randomization of the initial field is introduced as perturbations around the average value with a set amplitude of random noise whose value is changed. In our LES simulations (Figure 16), altering this initial randomization results in general variability in LWP peaks (around $10~g/m^2$) and precipitation rates associated with Flowers, which can be attributed purely to this changing randomness in initial 3D fields. Interestingly, there is a notable lack of variation leading up to the formation of Flowers.

5. Summary and Discussion

In summary, the multi-model LES simulations successfully reproduced the Flowers observed in the region, despite variations in timing and length-scale compared to satellite imagery. The simulations showed clouds beginning to aggregate early on February 2nd, coinciding with a rapid increase in sea surface temperature from about 26°C to 26.5°C and surface wind speeds rising to around 9 m/s, which matched the typical environmental conditions associated with Flowers in the region (Bony et al., 2020). Consistent with the general observation of high Lower Tropospheric Stability (LTS) during Flowers (Schulz et al., 2021), the simulations showed an average LTS of around 17–18 K on February 2nd, prior to their emergence. Radiosonde data from earlier times indicate

RAGHUNATHAN ET AL. 23 of 29

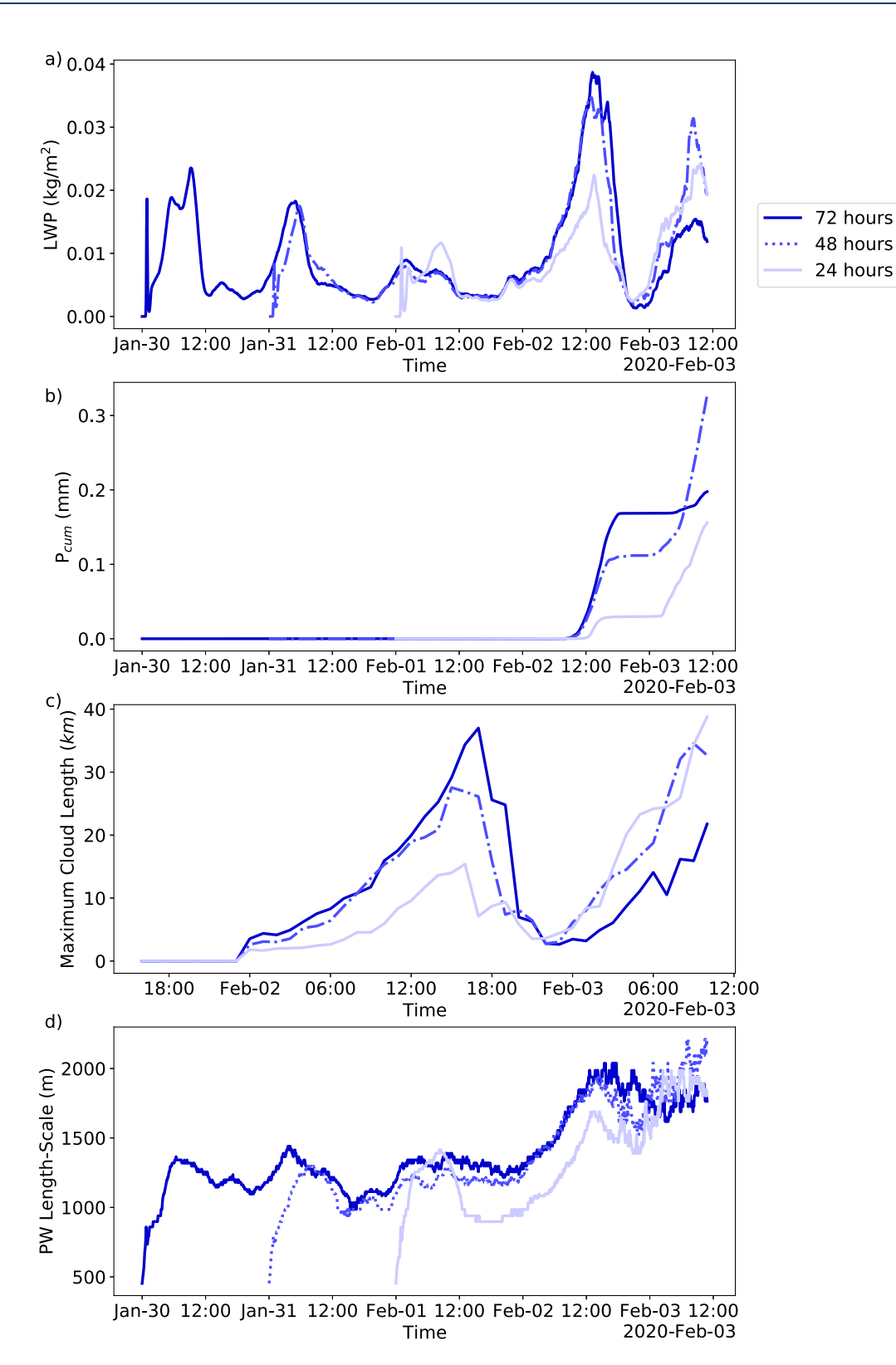


Figure 15. (a) Cloud Liquid water path (b) Cumulative total of Surface Precipitation based on average rain rate over the entire simulation domain, (c) maximum cloud length derived from tracked individual cloud structures based on 2d liquid water path fields with LWP $> 0.01 \text{ kg/m}^2$ for MicroHH simulations with varying lead time to 00 UTC on February 2nd and (d) Length scale of total precipitable water within which 2/3 of its total variance resides. The dashed lines here indicate the simulation which was used in the inter-comparison.

RAGHUNATHAN ET AL. 24 of 29

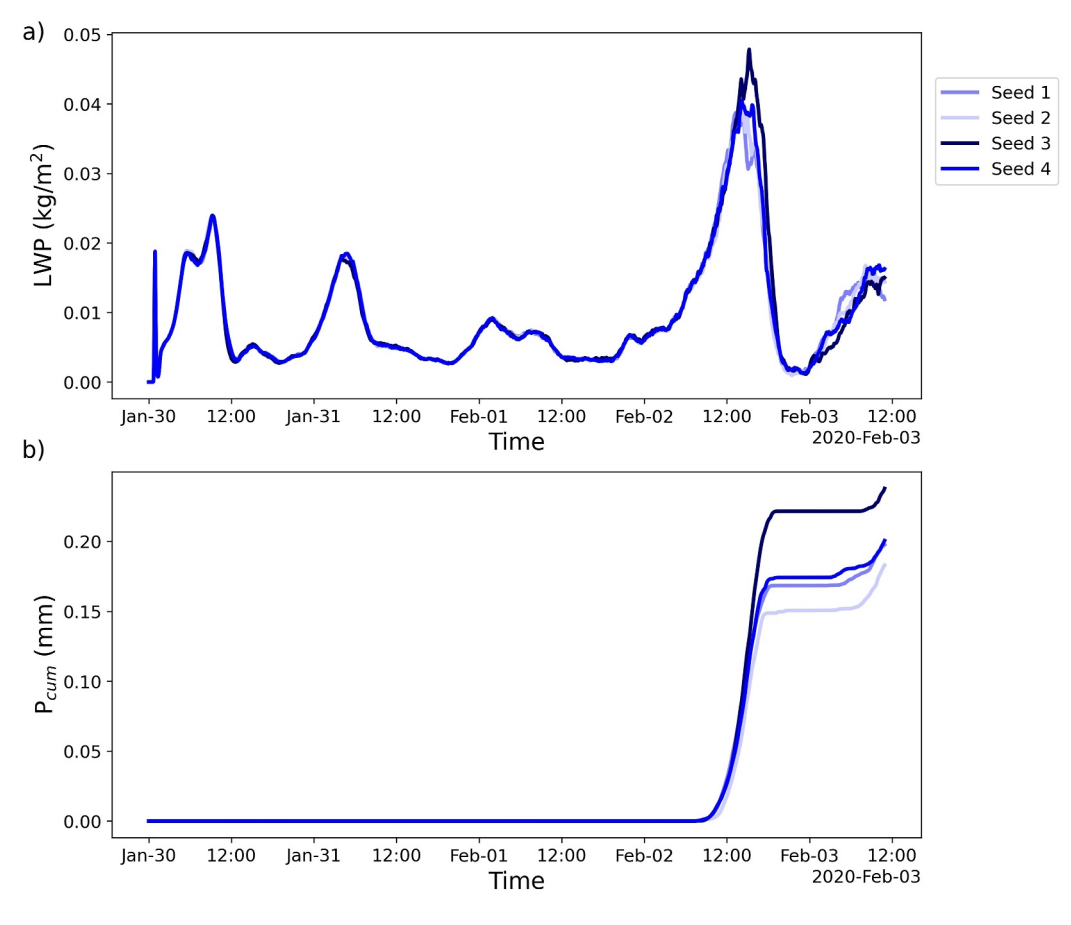


Figure 16. (a) Cloud Liquid water path (b) Cumulative total of surface precipitation based on average rain rate over the entire simulation domain for ensemble of cases with just variations in initial field randomization for February 2nd case with a 3-day lead time.

the presence of a strong stable layer around 2.5 km in height, which consistently appears at various times through the day. As the simulation trajectory draws closer to the RHB vessel a pronounced stable layer becomes evident in the simulation output as well. With growth in boundary layer height, the cloud tops reach this height and soon we witness growth in size of cloud clusters. This is possibly a result of strong stable layer preventing strong updrafts from rising further, causing moisture to be transported laterally below or within the inversion layer and creating an outflow region. This is detected in several models as an increase in U and V velocities around the stable layer. However, by 17 UTC, this strong outflow dissipates, potentially due to the cessation of strong updrafts. While local forcing may induce a strong stable layer and aid in the formation of Flowers, the subsequent sustenance and dissipation of Flower clouds in individual model simulations seems to result from how each model's microphysics responds to the locally forced thermodynamic properties. This might explain why, despite a strong alignment in thermodynamic and cloud properties leading up to Flower formation, there are significant differences in the sustenance and decay phases across models.

Analyzing the cloud vertical structure during Flower development reveals a mismatch in timing between the increase in cloud liquid water content and the onset of cloud cluster growth. Deeper examination of cloud cover vertical profiles shows the emergence of thin near-stable-layer clouds in the outflow region of Flower cloud clusters. The joint probability density of cloud base and cloud top heights exhibits three distinct maxima, with changes in their probability density indicating different stages in the evolution of the Flower cloud state. One of these peaks, linked to deeper clouds with bases near the lifting condensation level and tops near the inversion, is associated with stronger updrafts that deliver moisture to the inversion layer and also to the grid columns with large liquid water paths that contribute much of the precipitation in these simulations. The reduced probability densities of these deeper clouds align with the dissipation stage of Flower, likely caused by a reduction in moisture

RAGHUNATHAN ET AL. 25 of 29

supply to the thinning anvil top as the deeper clouds fade. Analysis of cloud size distributions reveals consistent cloud number densities across simulations, with a notable increase in the number of clouds larger than 5 km during the Flower phase compared to predictions from the power law.

The findings from Flower sensitivity to CDNC align with prior studies in showing decreased rain rates and cold pool activity with higher CDNC but reveal unique behavior at both the extremes in CDNC values, highlighting the role of delayed precipitation in fostering cloud aggregation. Simulations initialized with over 48 hr of lead time produced larger Flower cloud structures with consistent length scales, while a shorter lead time resulted in smaller-scale clouds due to insufficient moisture convergence by the time favorable conditions arose. Variations in the initial randomization of fields in LES simulations introduce localized differences that primarily affect LWP peaks and precipitation rates during Flower formation, though minimal variability is observed beforehand.

To summarize, beyond a general intercomparison of thermodynamic properties and cloud structure across LES models and observations, we have explored how the cloud structure changes over the course of organized Flower state. Key findings from this include: the role of deeper cloud columns associated with cloudy updrafts in maintaining the Flowers; a consistent lead of LWP and rain rate peaks before the full development of Flower cloud; most of the precipitation originating from columns with total LWP exceeding 1 kg/m²; the simulation with the highest CDNC, despite showing weaker cold pools and lower precipitation rates, producing the largest Flower by area, breaking the trend seen in the intermediate CDNC cases; and finally, the importance of moisture convergence within the domain in initiating and growing Flower cloud structures, as evident from simulations with different lead times.

Overall, these Lagrangian simulations of Flower clouds demonstrated a strong level of consistency both across models and with observational data, even when forced with ERA5 data. The Lagrangian framework offers advantages over Eulerian approaches by allowing us to disregard advective processes that are not central to the study, focusing instead on the development of clouds and organization within an airmass as it is carried by the trade winds. This approach also enables the separation of atmospheric dynamics from local sea surface interactions, providing a clearer view of atmospheric behavior. However, Lagrangian simulations do have limitations; by design, they can properly track only one atmospheric level, requiring relative advection adjustments for other levels in relation to the base state. This is in contrast to intercomparisons of Eulerian simulations in larger domains that use open boundary conditions.

For future work, we observe that microphysical process details significantly influence simulation outcomes, even within observational uncertainty bounds, suggesting that a deeper understanding of these processes, supported by observational constraints, would enhance our insights. For example, Lagrangian (airplane-based) observations of cloud droplet number concentration (CDNC) and cloud condensation nuclei (CCN), with complementary remote sensing retrievals of precipitation and cloud/rain water paths, could provide valuable data. Additionally, we intend to examine cold pools further and explore whether models handle weakly forced convection as effectively. By investigating different organizational modes and patterns in a similar framework, we aim to extend this approach to a broader range of convective processes.

Conflict of Interest

The authors declare no conflicts of interest relevant to this study.

Data Availability Statement

Data files and the Jupyter notebooks used for making the plots for the paper are available at Raghunathan et al. (2024). The code (Lagtraj) used for generating trajectories and finding ERA5 initial sounding, advection and sea surface temperature profiles along the trajectory can be found at https://github.com/EUREC4A-UK/lagtraj. Also, two of the LES codes used in this study are maintained as open-source codes (DALES: https://github.com/microhh/microhh). A specialized version of LES code MONC, based on revision r10514, which is capable to read Lagtraj input can be found at https://github.com/sjboeing/monc/releases/tag/eurec4a_intercomparison_submit.

RAGHUNATHAN ET AL. 26 of 29



Journal of Advances in Modeling Earth Systems

10.1029/2024MS004864

Acknowledgments

Some of the simulations and all of the analysis were performed on the Ohio Supercomputer Center Center (1987) and on systems provided by the Cleveland State University ADAM Research Center. Computing resources were also provided by the Derecho (https://doi.org/10.5065/ qx9a-pg09) and Cheyenne (https://doi.org/ 10.5065/D6RX99HX) system provided by the NSF National Center for Atmospheric Research (NCAR), sponsored by the National Science Foundation; and the ARCHER2 UK National Supercomputing Service (https://www.archer2.ac.uk), supported by NERC Grant NE/S015868/1. This research was supported by the U.S. Department of Energy's Atmospheric System Research, an Office of Science Biological and Environmental Research program, under Grants DE-SC0017999, DE-SC0022126 and National Science Foundation Grant AGS-1938108 (PNB). We also gratefully acknowledge funding by the DFG (German Research Foundation) for project POPC4OM with number 434804401 and the Gauss Centre for Supercomputing e.V. (www.gausscentre.eu) for providing computing time for projects RCONGM and HR-AFC through the John von Neumann Institute for Computing (NIC) on the GCS Supercomputer JUWELS at Jülich Supercomputing Centre (JSC). We thank the reviewers for their thoughtful and constructive feedback, which significantly helped improve the clarity and quality of this manuscript.

References

- Alinaghi, P., Jansson, F., Blázquez, D. A., & Glassmeier, F. (2024). Cold pools mediate mesoscale adjustments of trade-cumulus fields to changes in cloud-droplet number concentration. EGUsphere, 1–26. https://doi.org/10.5194/egusphere-2024-3501
- Asselin, R. (1972). Frequency filter for time integrations. *Monthly Weather Review*, 100(6), 487–490. https://doi.org/10.1175/1520-0493(1972) 100<0487:fffti>2.3.co;2
- Bannon, P. R., Chagnon, J. M., & James, R. P. (2006). Mass conservation and the anelastic approximation. *Monthly Weather Review*, 134(10), 2989–3005. https://doi.org/10.1175/mwr3228.1
- Beesley, J., Bretherton, C., Jakob, C., Andreas, E., Intrieri, J., & Uttal, T. (2000). A comparison of cloud and boundary layer variables in the ECMWF forecast model with observations at surface heat budget of the Arctic Ocean (SHEBA) ice camp. *Journal of Geophysical Research*, 105(D10), 12337–12349. https://doi.org/10.1029/2000jd900079
- Blossey, P. N., Bretherton, C. S., Cheng, A., Endo, S., Heus, T., Lock, A. P., & van der Dussen, J. J. (2016). CGILS Phase 2 LES intercomparison of response of subtropical marine low cloud regimes to CO₂ quadrupling and a CMIP 3 composite forcing change. *Journal of Advances in Modeling Earth Systems*, 8(4), 1714–1726. https://doi.org/10.1002/2016MS000765
- Bony, S., & Dufresne, J.-L. (2005). Marine boundary layer clouds at the heart of tropical cloud feedback uncertainties in climate models. Geophysical Research Letters, 32(20), L20806. https://doi.org/10.1029/2005g1023851
- Bony, S., Schulz, H., Vial, J., & Stevens, B. (2020). Sugar, gravel, fish, and flowers: Dependence of mesoscale patterns of trade-wind clouds on environmental conditions. *Geophysical Research Letters*, 47(7), e2019GL085988. https://doi.org/10.1029/2019GL085988
- Bretherton, C. S., & Blossey, P. N. (2014). Low cloud reduction in a greenhouse-warmed climate: Results from Lagrangian LES of a subtropical marine cloudiness transition. *Journal of Advances in Modeling Earth Systems*, 6(1), 91–114. https://doi.org/10.1002/2013MS000250
- Bretherton, C. S., & Blossey, P. N. (2017). Understanding mesoscale aggregation of shallow cumulus convection using large-eddy simulation. Journal of Advances in Modeling Earth Systems, 9(8), 2798–2821. https://doi.org/10.1002/2017MS000981
- Bretherton, C. S., Krueger, S. K., Wyant, M. C., Bechtold, P., Van Meijgaard, E., Stevens, B., & Teixeira, J. (1999). A GCSS boundary-layer cloud model intercomparison study of the first ASTEX Lagrangian experiment. *Boundary-Layer Meteorology*, 93(3), 341–380. https://doi.org/10.1023/A:1002005429969
- Brown, A. R., Derbyshire, S., & Mason, P. J. (1994). Large-eddy simulation of stable atmospheric boundary layers with a revised stochastic subgrid model. *Quarterly Journal of the Royal Meteorological Society*, 120(520), 1485–1512. https://doi.org/10.1256/smsqj.52003
- Brown, N., Weiland, M., Hill, A., Shipway, B., Maynard, C., Allen, T., & Rezny, M. (2015). A highly scalable Met Office NERC cloud model. In Exascale Applications and Software Conference 2015.
- Cahalan, R. F., & Joseph, J. H. (1989). Fractal statistics of cloud fields. *Monthly Weather Review*, 117(2), 261–272. https://doi.org/10.1175/1520-0493(1989)117<0261:fsocf>2.0.co;2
- Chandra, A. S., Kollias, P., & Albrecht, B. A. (2013). Multiyear summertime observations of daytime fair-weather cumuli at the arm southern Great Plains facility. *Journal of Climate*, 26(24), 10031–10050. https://doi.org/10.1175/jcli-d-12-00223.1
- Cui, Z., Blyth, A., Burton, R., Bony, S., Böing, S., Gadian, A., & Denby, L. (2023). Life cycle of a flower cloud system during the EUREC⁴A a field campaign. *EGUsphere*, 1–47. https://doi.org/10.5194/egusphere-2023-1999
- Dauhut, T., Couvreux, F., Bouniol, D., Beucher, F., Volkmer, L., Pörtge, V., et al. (2023). Flower trade-wind clouds are shallow mesoscale convective systems. *Quarterly Journal of the Royal Meteorological Society*, 149(750), 325–347. https://doi.org/10.1002/qj.4409
- de Roode, S. R., Duynkerke, P. G., & Jonker, H. J. (2004). Large-eddy simulation: How large is large enough? *Journal of the Atmospheric Sciences*, 61(4), 403–421. https://doi.org/10.1175/1520-0469(2004)061<0403:lshli|>2.0.co;2
- de Roode, S. R., Frederikse, T., Siebesma, A. P., Ackerman, A. S., Chylik, J., Field, P. R., et al. (2019). Turbulent transport in the gray zone: A large eddy model intercomparison study of the constrain cold air outbreak case. *Journal of Advances in Modeling Earth Systems*, 11(3), 597–623. https://doi.org/10.1029/2018ms001443
- de Roode, S. R., Sandu, I., Van Der Dussen, J. J., Ackerman, A. S., Blossey, P., Jarecka, D., et al. (2016). Large-eddy simulations of EUCLIPSE–GASS Lagrangian stratocumulus-to-cumulus transitions: Mean state, turbulence, and decoupling. *Journal of the Atmospheric Sciences*, 73(6), 2485–2508. https://doi.org/10.1175/JAS-D-15-0215.1
- Drager, A. J., & van den Heever, S. C. (2017). Characterizing convective cold pools. *Journal of Advances in Modeling Earth Systems*, 9(2), 1091–1115. https://doi.org/10.1002/2016ms000788
- Dzambo, A. M., L'Ecuyer, T., Sinclair, K., Van Diedenhoven, B., Gupta, S., McFarquhar, G., et al. (2021). Joint cloud water path and rainwater path retrievals from airborne oracles observations. *Atmospheric Chemistry and Physics*, 21(7), 5513–5532. https://doi.org/10.5194/acp-21-5513-2021
- Edwards, J., & Slingo, A. (1996). Studies with a flexible new radiation code. I: Choosing a configuration for a large-scale model. *Quarterly Journal of the Royal Meteorological Society*, 122(531), 689–719. https://doi.org/10.1002/qj.49712253107
- Fairall, C. W., Bradley, E. F., Hare, J., Grachev, A. A., & Edson, J. B. (2003). Bulk parameterization of air–sea fluxes: Updates and verification for the coare algorithm. *Journal of Climate*, 16(4), 571–591. https://doi.org/10.1175/1520-0442(2003)016\0003051:BPOASF\00020.0.CO;2
- Feingold, G., Walko, R., Stevens, B., & Cotton, W. (1998). Simulations of marine stratocumulus using a new microphysical parameterization scheme. *Atmospheric Research*, 47, 505–528. https://doi.org/10.1016/s0169-8095(98)00058-1
- Field, P. R., Hill, A., Shipway, B., Furtado, K., Wilkinson, J., Miltenberger, A., et al. (2023). Implementation of a double moment cloud microphysics scheme in the UK met office regional numerical weather prediction model. *Quarterly Journal of the Royal Meteorological Society*, 149(752), 703–739. https://doi.org/10.1002/qj.4414
- Fildier, B., Peiffer, L. T., & Schulz, H. (2021). bfildier/eurec4a_movies: v1.0.0. Zenodo. https://doi.org/10.5281/zenodo.4777954
- George, G., Stevens, B., Bony, S., Pincus, R., Fairall, C., Schulz, H., et al. (2021). Joanne: Joint dropsonde observations of the atmosphere in Tropical North Atlantic meso-scale environments. *Earth System Science Data*, 13(11), 5253–5272. https://doi.org/10.5194/essd-13-5253-2021
- George, G., Stevens, B., Bony, S., Vogel, R., & Naumann, A. K. (2023). Widespread shallow mesoscale circulations observed in the trades. Nature Geoscience, 16(7), 584–589. https://doi.org/10.1038/s41561-023-01215-1
- Glenn, I. B., & Krueger, S. K. (2014). Downdrafts in the near cloud environment of deep convective updrafts. *Journal of Advances in Modeling Earth Systems*, 6(1), 1–8. https://doi.org/10.1002/2013ms000261
- Heus, T., van Heerwaarden, C. C., Jonker, H. J., Pier Siebesma, A., Axelsen, S., Van Den Dries, K., et al. (2010). Formulation of the Dutch Atmospheric Large-Eddy Simulation (DALES) and overview of its applications. *Geoscientific Model Development*, 3(2), 415–444. https://doi.org/10.5194/gmd-3-415-2010
- Iacono, M. J., Delamere, J. S., Mlawer, E. J., Shephard, M. W., Clough, S. A., & Collins, W. D. (2008). Radiative forcing by long-lived greenhouse gases: Calculations with the AER radiative transfer models. *Journal of Geophysical Research*, 113(D13). https://doi.org/10.1029/2008jd009944

RAGHUNATHAN ET AL. 27 of 29

- Janssens, M., de Arellano, J. V.-G., van Heerwaarden, C. C., de Roode, S. R., Siebesma, A. P., & Glassmeier, F. (2023a). Nonprecipitating shallow cumulus convection is intrinsically unstable to length scale growth. *Journal of the Atmospheric Sciences*, 80(3), 849–870. https://doi.org/10.1175/JAS-D-22-0111.1
- Janssens, M., Vilà-Guerau de Arellano, J., Van Heerwaarden, C. C., Van Stratum, B. J., De Roode, S. R., Siebesma, A. P., & Glassmeier, F. (2023b). The time scale of shallow convective self-aggregation in large-eddy simulations is sensitive to numerics. *Journal of Advances in Modeling Earth Systems*, 15(1), e2022MS003292. https://doi.org/10.1029/2022MS003292
- Jiang, H., Feingold, G., Jonsson, H. H., Lu, M.-L., Chuang, P. Y., Flagan, R. C., & Seinfeld, J. H. (2008). Statistical comparison of properties of simulated and observed cumulus clouds in the vicinity of Houston during the Gulf of Mexico atmospheric composition and climate study (GOMACCS). *Journal of Geophysical Research*, 113(D13). https://doi.org/10.1029/2007jd009304
- Kazil, J., Christensen, M. W., Abel, S. J., Yamaguchi, T., & Feingold, G. (2021). Realism of Lagrangian large eddy simulations driven by reanalysis meteorology: Tracking a pocket of open cells under a biomass burning aerosol layer. *Journal of Advances in Modeling Earth* Systems, 13(12), e2021MS002664. https://doi.org/10.1029/2021ms002664
- Kazil, J., Narenpitak, P., Yamaguchi, T., & Feingold, G. (2024). On climate change and trade cumulus organization. *Journal of Advances in Modeling Earth Systems*, 16(9), e2023MS004057. https://doi.org/10.1029/2023MS004057
- Khairoutdinov, M. F., & Randall, D. A. (2003). Cloud resolving modeling of the ARM summer 1997 IOP: Model formulation, results, uncertainties, and sensitivities. *Journal of the Atmospheric Sciences*, 60(4), 607–625. https://doi.org/10.1175/1520-0469(2003)060(0607: CRMOTA)2.0.CO;2
- Lebsock, M. D., L'Ecuyer, T. S., & Stephens, G. L. (2011). Detecting the ratio of rain and cloud water in low-latitude shallow marine clouds. Journal of Applied Meteorology and Climatology, 50(2), 419–432. https://doi.org/10.1175/2010JAMC2494.1
- Leonard, B., MacVean, M., & Lock, A. (1993). Positivity-preserving numerical schemes for multidimensional advection (Tech. Rep.). NASA Lewis Research Center. (NASA TM-106055).
- Lipps, F. B., & Hemler, R. S. (1982). A scale analysis of deep moist convection and some related numerical calculations. *Journal of the Atmospheric Sciences*, 39(10), 2192–2210. https://doi.org/10.1175/1520-0469(1982)039<2192:asaodm>2.0.co;2
- Malkus, J. S., & Riehl, H. (1964). Cloud structure and distributions over the tropical Pacific Ocean 1. Tellus, 16(3), 275–287. https://doi.org/10. 1111/j.2153-3490.1964.tb00167.x
- McClatchey, R. (1972). Optical properties of the atmosphere (No. 411). Air Force Cambridge Research Laboratories, Office of Aerospace
- Medeiros, B., & Nuijens, L. (2016). Clouds at Barbados are representative of clouds across the trade wind regions in observations and climate models. *Proceedings of the National Academy of Sciences of the United States of America*, 113(22), E3062–E3070. https://doi.org/10.1073/pnes_1521404113
- Mlawer, E. J., Taubman, S. J., Brown, P. D., Iacono, M. J., & Clough, S. A. (1997). Radiative transfer for inhomogeneous atmospheres: RRTM, a validated correlated-k model for the longwave. *Journal of Geophysical Research*, 102(D14), 16663–16682. https://doi.org/10.1029/97JD00237
- Monin, A. S., & Obukhov, A. M. (1954). Basic laws of trubulent mixing in the ground layer of the atmosphere. *Trudy Geologicheskiy Institut, Akademiya Nauk SSSR*, 151, 163–187.
- Morrison, H., Curry, J. A., & Khvorostyanov, V. I. (2005). A new double-moment microphysics parameterization for application in cloud and climate models. Part I: Description. *Journal of the Atmospheric Sciences*, 62(6), 1665–1677. https://doi.org/10.1175/JAS3446.1
- Muller, C., & Bony, S. (2015). What favors convective aggregation and why? Geophysical Research Letters, 42(13), 5626–5634. https://doi.org/10.1002/2015g1064260
- Narenpitak, P., Kazil, J., Yamaguchi, T., Quinn, P., & Feingold, G. (2021). From sugar to flowers: A transition of shallow cumulus organization during atomic. *Journal of Advances in Modeling Earth Systems*, 13(10), e2021MS002619. https://doi.org/10.1029/2021ms002619
- Neggers, R., Ackerman, A. S., Angevine, W., Bazile, E., Beau, I., Blossey, P., et al. (2017). Single-column model simulations of subtropical marine boundary-layer cloud transitions under weakening inversions. *Journal of Advances in Modeling Earth Systems*, 9(6), 2385–2412. https://doi.org/10.1002/2017MS001064
- Neggers, R., Duynkerke, P., & Rodts, S. (2003). Shallow cumulus convection: A validation of large-eddy simulation against aircraft and landsat observations. Quarterly Journal of the Royal Meteorological Society: A journal of the atmospheric sciences, applied meteorology and physical oceanography, 129(593), 2671–2696. https://doi.org/10.1256/qj.02.93
- Neggers, R., Griewank, P., & Heus, T. (2019). Power-law scaling in the internal variability of cumulus cloud size distributions due to subsampling and spatial organization. *Journal of the Atmospheric Sciences*, 76(6), 1489–1503. https://doi.org/10.1175/jas-d-18-0194.1
- Nugent, J. M., Turbeville, S., Bretherton, C. S., Blossey, P. N., & Ackerman, T. P. (2022). Tropical cirrus in global storm-resolving models: 1. Role of deep convection. Earth and Space Science, 9(2), e2021EA001965. https://doi.org/10.1029/2021EA001965
- Nuijens, L., & Siebesma, A. P. (2019). Boundary layer clouds and convection over subtropical oceans in our current and in a warmer climate. Current Climate Change Reports, 5(2), 80–94. https://doi.org/10.1007/s40641-019-00126-x
- Ohio supercomputer center. (1987). Ohio supercomputer center. Retrieved from http://osc.edu/ark:/19495/f5s1ph73
- Piacsek, S. A., & Williams, G. P. (1970). Conservation properties of convection difference schemes. *Journal of Computational Physics*, 6(3), 392–405. https://doi.org/10.1016/0021-9991(70)90038-0
- Pincus, R., & Stevens, B. (2009). Monte Carlo spectral integration: A consistent approximation for radiative transfer in large eddy simulations. Journal of Advances in Modeling Earth Systems, 1(2). https://doi.org/10.3894/james.2009.1.1
- Quinn, P. K., Thompson, E. J., Coffman, D. J., Baidar, S., Bariteau, L., Bates, T. S., et al. (2021). Measurements from the RV Ronald H. Brown and related platforms as part of the Atlantic tradewind ocean-atmosphere mesoscale interaction campaign (atomic). Earth System Science Data, 13(4), 1759–1790. https://doi.org/10.5194/essd-13-1759-2021
- Raghunathan, G. N., Blossey, P., Boeing, S., Denby, L., Ghazayel, S., Heus, T., et al. (2024). Multi-LES code output of Flower-type organized convection on 02 February, 2020—0-1D Files. Zenodo. https://doi.org/10.5281/zenodo.14218605
- Rasp, S., Schulz, H., Bony, S., & Stevens, B. (2020). Combining crowdsourcing and deep learning to explore the mesoscale organization of shallow convection. Bulletin of the American Meteorological Society, 101(11), E1980–E1995. https://doi.org/10.1175/bams-d-19-0324.1
- Royer, H. M., Pöhlker, M. L., Krüger, O., Blades, E., Sealy, P., Lata, N. N., et al. (2023). African smoke particles act as cloud condensation nuclei in the wintertime tropical North Atlantic boundary layer over Barbados. Atmospheric Chemistry and Physics, 23(2), 981–998. https://doi.org/ 10.5194/acp-23-981-2023
- Saffin, L., Lock, A., Tomassini, L., Blyth, A., Böing, S., Denby, L., & Marsham, J. (2023). Kilometer-scale simulations of trade-wind cumulus capture processes of mesoscale organization. *Journal of Advances in Modeling Earth Systems*, 15(3), e2022MS003295. https://doi.org/10.1029/2022ms003295
- Sandu, I., & Stevens, B. (2011). On the factors modulating the stratocumulus to cumulus transitions. *Journal of the Atmospheric Sciences*, 68(9), 1865–1881. https://doi.org/10.1175/2011JAS3614.1

RAGHUNATHAN ET AL. 28 of 29



Journal of Advances in Modeling Earth Systems

- 10.1029/2024MS004864
- Savazzi, A. C. M., Nuijens, L., Sandu, I., George, G., & Bechtold, P. (2022). The representation of the trade winds in ECMWF forecasts and reanalyses during EUREC⁴A. *Atmospheric Chemistry and Physics*, 22(19), 13049–13066. https://doi.org/10.5194/acp-22-13049-2022
- Savic-Jovcic, V., & Stevens, B. (2008). The structure and mesoscale organization of precipitating stratocumulus. *Journal of the Atmospheric Sciences*, 65(5), 1587–1605. https://doi.org/10.1175/2007JAS2456.1
- Schulz, H., Eastman, R., & Stevens, B. (2021). Characterization and evolution of organized shallow convection in the downstream North Atlantic trades. *Journal of Geophysical Research: Atmospheres*, 126(17), e2021JD034575. https://doi.org/10.1029/2021JD034575
- Schulz, H., & Stevens, B. (2023). Evaluating large-domain, hecto-meter, large-eddy simulations of trade-wind clouds using EUREC⁴A data. Journal of Advances in Modeling Earth Systems, 15(10), e2023MS003648. https://doi.org/10.1029/2023ms003648
- Seifert, A., & Beheng, K. D. (2006). A two-moment cloud microphysics parameterization for mixed-phase clouds. Part 1: Model description. Meteorology and Atmospheric Physics, 92(1), 45–66. https://doi.org/10.1007/s00703-005-0112-4
- Seifert, A., & Heus, T. (2013). Large-eddy simulation of organized precipitating trade wind cumulus clouds. *Atmospheric Chemistry and Physics*, 13(11), 5631–5645. https://doi.org/10.5194/acp-13-5631-2013
- Seifert, A., Heus, T., Pincus, R., & Stevens, B. (2015). Large-eddy simulation of the transient and near-equilibrium behavior of precipitating shallow convection. *Journal of Advances in Modeling Earth Systems*, 7(4), 1918–1937. https://doi.org/10.1002/2015ms000489
- Siebesma, A. P., Bretherton, C. S., Brown, A., Chlond, A., Cuxart, J., Duynkerke, P. G., et al. (2003). A large eddy simulation intercomparison study of shallow cumulus convection. *Journal of the Atmospheric Sciences*, 60(10), 1201–1219. https://doi.org/10.1175/1520-0469(2003)60 (1201:ALESIS)2.0.CO:2
- Stevens, B., Bony, S., Brogniez, H., Hentgen, L., Hohenegger, C., Kiemle, C., et al. (2020). Sugar, gravel, fish and flowers: Mesoscale cloud patterns in the trade winds. *Quarterly Journal of the Royal Meteorological Society*, 146(726), 141–152. https://doi.org/10.1002/qj.3662
- Stevens, B., Bony, S., Farrell, D., Ament, F., Blyth, A., Fairall, C., et al. (2021). EUREC⁴A. Earth System Science Data, 13(8), 4067–4119. https://doi.org/10.5194/essd-13-4067-2021
- Touzé-Peiffer, L., Vogel, R., & Rochetin, N. (2022). Cold pools observed during EUREC⁴A: Detection and characterization from atmospheric soundings. *Journal of Applied Meteorology and Climatology*, 61(5), 593–610. https://doi.org/10.1175/jamc-d-21-0048.1
- Van der Dussen, J. J., De Roode, S. R., Ackerman, A. S., Blossey, P. N., Bretherton, C. S., Kurowski, M. J., et al. (2013). The GASS/EUCLIPSE model intercomparison of the stratocumulus transition as observed during ASTEX: Les results. *Journal of Advances in Modeling Earth Systems*, 5(3), 483–499. https://doi.org/10.1002/jame.20033
- Van Heerwaarden, C. C., Van Stratum, B. J., Heus, T., Gibbs, J. A., Fedorovich, E., & Mellado, J. P. (2017). MicroHH 1.0: A computational fluid dynamics code for direct numerical simulation and large-eddy simulation of atmospheric boundary layer flows. Geoscientific Model Development, 10(8), 3145–3165. https://doi.org/10.5194/gmd-10-3145-2017
- VanZanten, M. C., Stevens, B., Nuijens, L., Siebesma, A. P., Ackerman, A., Burnet, F., et al. (2011). Controls on precipitation and cloudiness in simulations of trade-wind cumulus as observed during Rico. *Journal of Advances in Modeling Earth Systems*, 3(2). https://doi.org/10.1029/
- Vial, J., Bony, S., Stevens, B., & Vogel, R. (2018). Mechanisms and model diversity of trade-wind shallow cumulus cloud feedbacks: A review. In Shallow clouds, water vapor, circulation, and climate sensitivity (pp. 159–181). https://doi.org/10.1007/978-3-319-77273-8_8
- Vogel, R., Konow, H., Schulz, H., & Zuidema, P. (2021a). A climatology of trade-wind cumulus cold pools and their link to mesoscale cloud organization. Atmospheric Chemistry and Physics, 21(21), 16609–16630. https://doi.org/10.5194/acp-21-16609-2021
- Vogel, R., Konow, H., Schulz, H., & Zuidema, P. (2021b). A climatology of trade-wind cumulus cold pools and their link to mesoscale cloud organization. Atmospheric Chemistry and Physics, 21(21), 16609–16630. https://doi.org/10.5194/acp-21-16609-2021
- Vogel, R., Nuijens, L., & Stevens, B. (2016). The role of precipitation and spatial organization in the response of trade-wind clouds to warming. Journal of Advances in Modeling Earth Systems, 8(2), 843–862. https://doi.org/10.1002/2015ms000568
- Walsh, J., & Watterson, J. (1993). Fractal analysis of fracture patterns using the standard box-counting technique: Valid and invalid methodologies. *Journal of Structural Geology*, 15(12), 1509–1512. https://doi.org/10.1016/0191-8141(93)90010-8
- Wang, H., & Feingold, G. (2009). Modeling mesoscale cellular structures and drizzle in marine stratocumulus. Part I: Impact of drizzle on the formation and evolution of open cells. *Journal of the Atmospheric Sciences*, 66(11), 3237–3256. https://doi.org/10.1175/2009jas3022.1
- Yamaguchi, T., Feingold, G., & Kazil, J. (2017). Stratocumulus to cumulus transition by drizzle. *Journal of Advances in Modeling Earth Systems*, 9(6), 2333–2349. https://doi.org/10.1002/2017ms001104
- Yamaguchi, T., Feingold, G., & Kazil, J. (2019). Aerosol-cloud interactions in trade wind cumulus clouds and the role of vertical wind shear. Journal of Geophysical Research: Atmospheres. 124(22), 12244–12261, https://doi.org/10.1029/2019JD031073
- Yamaguchi, T., Randall, D. A., & Khairoutdinov, M. F. (2011). Cloud modeling tests of the ultimate–macho scalar advection scheme. Monthly Weather Review, 139(10), 3248–3264. https://doi.org/10.1175/MWR-D-10-05044.1
- Zuidema, P., Li, Z., Hill, R. J., Bariteau, L., Rilling, B., Fairall, C., et al. (2012). On trade wind cumulus cold pools. *Journal of the Atmospheric Sciences*, 69(1), 258–280. https://doi.org/10.1175/jas-d-11-0143.1

RAGHUNATHAN ET AL. 29 of 29